

Chapter 2

Analytical Method of EMAT Based on Lorentz Force Mechanism

The energy conversion mechanism of EMAT that is used in non-ferromagnetic metal material is the *Lorentz force* mechanism. The corresponding EMAT is called the *Lorentz force*-based EMAT. For the *Lorentz force*-based EMAT, there is a relatively complete ultrasonic mathematic model that is used to describe the excitation and receiving of EMAT. But because of the coupling between the electromagnetic field and mechanical field in the complete energy conversion process, it can be very difficult to achieve its numerical simulation. In EMAT, the spiral coil and meander coil are widely used, and with the improvement of the coil's production process, those two kinds of coils are generally designed as the complex structures of multilayer or multisplit. Another alternative approach for theoretical analysis is making analytical models of EMAT with those two kinds of coil structure, and calculating its coil impedance and pulse response. Considering that most excitation power supplies of EMAT are voltage-sourced, while almost all the analysis of the existing mathematical models use current excitation to do the analysis of EMAT, it is necessary to propose the analytical method of EMAT under the excitation of impulse voltage. This chapter mainly concerns the simulation analysis of the entire process of EMAT based on the *Lorentz force* mechanism finite element method. The analytical calculation method of the EMAT has the spiral coil and meander coil structure under the excitation of pulsed voltage.

2.1 Multifield Coupling Equation of EMAT Based on Lorentz Force Mechanism

The EMAT based on the *Lorentz force* mechanism consists of the biasing magnet, coil, and non-ferromagnetic specimen. The biasing magnet is used to provide a bias magnetic field, the coil is used to produce a pulsed magnetic field, and the specimen is used for the excitation and reception of the ultrasonic waves. The static magnetic

field, pulsed eddy current field, and mechanical field are involved in the multifield coupling. The numerical simulation analysis of the whole energy conversion process of EMAT means solving the multifield coupling problem. In this work, the equations used to describe the physical fields that include the excitation and receiving processes of EMAT ultrasonic waves are given first.

2.1.1 Magnetic Field Equation of a Permanent Magnet

The magnetic field generated by a permanent magnet belongs to the static magnetic field. In the magnetic field of a permanent magnet, there is no free current, which means the current density is $J = 0$, as expressed in (2.1).

$$\nabla \times H = 0 \quad (2.1)$$

In the above equation, H is the magnetic field intensity and can be represented as the gradient of a scalar function, as shown in (2.2).

$$H = -\nabla \varphi_m \quad (2.2)$$

In the above equation, φ_m is the scalar magnetic potential.

Considering the existence of the permanent magnet, (2.3) can be obtained.

$$B = \mu H + \mu_0 M_0 = \mu H + B_r \quad (2.3)$$

In the above equation, μ is the magnetic permeability of the magnetic medium; μ_0 is the magnetic permeability of the vacuum, M_0 is the residual magnetization; B is the intensity of the magnetic induction, and B_r is the residual magnetic intensity in the permanent magnet.

Substituting (2.2) into (2.3), from $\nabla \cdot B = 0$, (2.4) can be obtained.

$$\mu \nabla^2 \varphi_m = -\mu_0 \nabla \cdot M_0 \quad (2.4)$$

According to the magnetic charge model of the computational electromagnetism, the spatial magnetic field is produced by magnetic charge. The magnetic field generated in the space by a permanent magnet with a limited size can be taken as the superposition of the magnetic field generated in the space by the magnetic charge that is distributed with a certain rule; that is, the permanent magnet with a limited size can be taken as the magnetic charge distribution with a certain rule. The relationship is shown in (2.5).

$$\rho_m = -\mu_0 \nabla \cdot M_0 \quad (2.5)$$

In the above equation, ρ_m is the magnetic charge density; for the permanent magnet magnetizing uniformly with a certain direction, M_0 is a constant vector. Therefore, (2.6) can be obtained.

$$\rho_m = 0 \quad (2.6)$$

For the permanent magnet with a uniform magnetization, there is no body magnetic charge density, only the surface magnetic charge density σ_m exists. Then, (2.4) can be expressed by (2.7).

$$\mu \nabla^2 \varphi_m = 0 \quad (2.7)$$

The interface condition between the magnetic pole surface of the permanent magnet and any other medium is listed in (2.8).

$$\sigma_m = \mu_0 M_0 \cdot n \quad (2.8)$$

2.1.2 Dynamic Magnetic Field Equation of the Pulsed Eddy Current [1]

There is no free charge in a system that consists of an EMAT coil and a specimen. If the effect of displacement current density is overlooked, the dynamic magnetic field of the pulsed eddy current can be expressed by (2.9).

$$\frac{1}{\mu} \nabla^2 A - \sigma \frac{\partial A}{\partial t} = -J_s \quad (2.9)$$

In the above equation, A is the vector magnetic potential; σ represents the material's conductivity, and J_s is the density of the source current.

The right part of (2.9) is the density of the source current. In the simulation of EMAT, the excitation current and voltage are generally provided. The current density should be determined by the given value of electric current or voltage. When the coil's skin effect and proximity effect can be neglected, the distribution of the average current density in the coil can be approximately solved by electric current, as shown in (2.10).

$$J_s = \frac{i}{S} \quad (2.10)$$

In the above equation, i is the total current and S is the cross-area of the coil conductor.

Because the excitation frequency applied in the EMAT's coil can be very high from KHz to MHz and the distance between the coil conductors, as well as that from

the coil conductor to specimen, are all very small, the coil's skin effect, proximity effect, and eddy effect are all very significant. It is unnecessary to figure out the accuracy of the theoretical calculation that can be reduced if those effects discussed above are overlooked. Actually, the total current density is expressed in (2.11).

$$J_t = J_s + J_e = J_s - \sigma \frac{\partial A}{\partial t} \quad (2.11)$$

The total current can be expressed by (2.12).

$$\iint_S J_t ds = i \quad (2.12)$$

Then, (2.13) can be obtained.

$$J_s = \frac{i}{S} + \frac{1}{S} \iint_S \sigma \frac{\partial A}{\partial t} ds \quad (2.13)$$

And (2.14) can be obtained by substituting (2.13) into (2.9).

$$\frac{1}{\mu} \nabla^2 A - \sigma \frac{\partial A}{\partial t} + \frac{1}{S} \iint_S \sigma \frac{\partial A}{\partial t} ds = -\frac{i}{S} \quad (2.14)$$

The relationship between E (the electric field intensity of each location) and vector magnetic potential is expressed in (2.15).

$$E = -\frac{\partial A}{\partial t} \quad (2.15)$$

The eddy current density inside the coil and specimen is expressed in (2.16).

$$J_e = -\sigma \frac{\partial A}{\partial t} \quad (2.16)$$

From the definition of *Lorentz force*, the force density in the skin depth of the surface of a non-ferromagnetic specimen is related to the magnitude of the static magnetic field provided by the biasing magnet and the eddy current in the surface of the non-ferromagnetic conductor; it can be expressed by (2.17).

$$f_L = B_0 \times J_e \quad (2.17)$$

In the previous literature, the static magnetic field has uniform distribution. So the force on the surface of the non-ferromagnetic specimen extends in one single-direction, but this does not conform to the specific circumstances. In the practical application of EMAT, the value and direction of the static magnetic field

provided by the permanent magnet are not uniform nor in a single-direction; thus, it will inevitably bring errors if the static magnetic field is assumed to have uniform distribution and one single direction.

The boundary condition must be satisfied on the outer boundary. That is the vector magnetic potential $A_z = 0$.

In the interface of two kinds of magnetic medium, the following interface conditions listed in (2.18) are satisfied.

$$A_i = A_{i+1} \quad (2.18)$$

$$\frac{1}{\mu_i} (\nabla \times A_i)_t - \frac{1}{\mu_{i+1}} (\nabla \times A_{i+1})_t = J_{si} \quad (2.19)$$

In the above equations, subscript i represents the adjacent magnetic medium; subscript t represents the tangential direction of the interface, and J_{si} is the surface current density in the adjacent interface.

2.1.3 Motion Equation of Particle in the Specimen

The tested specimen is isotropic material, so it can be assumed as having linear elasticity and continuity. The elastic deformation occurs inside the specimen under the *Lorentz force*. The motion equation in the specimen is expressed in (2.20).

$$\nabla \cdot \sigma + f_L = \rho \frac{\partial^2 u}{\partial t^2} \quad (2.20)$$

In the above equation, σ is the stress tensor; u is the displacement matrix, and ρ is the specimen's bulk density.

Considering the relationship between σ and u , (2.20) can be expressed using the displacement, as in (2.21).

$$G \nabla^2 u + (G + k) \nabla (\nabla \cdot u) + f_L = \rho \frac{\partial^2 u}{\partial t^2} \quad (2.21)$$

In the above equation, G and k are *Lame constants*.

The traction-free boundary condition should be satisfied such that stress is zero and the strain is not zero on the surface of the specimen.

2.1.4 Receiving Equation of Ultrasonic Signal

When the ultrasonic wave in the specimen propagates to the receiving coil of EMAT, the charged particle will generate a dynamic current under the function of the external bias magnetic field; its current density is expressed in (2.22).

$$J_L = \sigma v \times B_0 \quad (2.22)$$

The current density in the specimen will generate a dynamic magnetic field inside and around the specimen. The coil of EMAT in the dynamic magnetic field will generate an induced electromotive force, which is the coil's receiving signal.

In the signal receiving process of the coil, the magnetic field in the solving area is provided by the eddy current density in the specimen and the source current density. Generally, the receiving coil is in an open circuit state and the total current of the receiving coil is zero. The governing equation satisfied in the area of the receiving coil and specimen can be expressed in (2.23).

$$-\frac{1}{\mu} \nabla^2 A + \sigma \frac{\partial A}{\partial t} - \frac{\sigma}{S} \frac{\partial}{\partial t} \iint_{\Omega_c} A ds = J_L \quad (2.23)$$

After solving the vector magnetic potential of each region using the above equation, the induced electromotive force of the coil can be calculated. The induced electric field in the coil can be expressed by (2.24).

$$E = -\frac{\partial A}{\partial t} \quad (2.24)$$

The conductor's electromotive force at some point of the coil can be obtained by using the line integral of the electric field intensity, expressed in (2.25).

$$V_{\text{pout}} = \int_l -\frac{\partial A}{\partial t} \cdot dl \quad (2.25)$$

Thus, the output voltage of the coil can be obtained by averaging the electromotive force of the point conductors in the coil, expressed in (2.26).

$$V_{\text{out}} = \frac{\int_{\Omega} V_{\text{pout}} d\Omega}{\int_{\Omega} d\Omega} \quad (2.26)$$

2.2 The Weak Form of the Coupling Field Equations

The analysis and simulation of the EMAT based on the Lorentz force mechanism aim at the specific physical model in combination with the corresponding boundary condition, solving the partial differential equations (2.7), (2.14), (2.21), and (2.23). The finite element method is an effective numerical method to solve this problem. When it comes to solving those equations using the finite element method, in fact, the solutions are the weak solutions, also referred to as the “weak form.” Thus, it is necessary to derive the weak form of the above equations, that is, to derive the weak forms of (2.7), (2.14), and (2.21) based on the principle of virtual displacement. Since the weak forms of (2.23) and (2.14) are similar to each other, they will not be given any more. According to the differences in the EMAT’s structure in the analytical process, the weak form of various field equations under the two-dimensional *Cartesian coordinate system* and axisymmetric coordinate system is needed, which are derived, respectively, as below.

2.2.1 The Weak Form of Coupled Equations Under Two-Dimensional Cartesian Coordinates

In the finite element analysis of EMAT, where the coil consists of linear conductors (such as the meander coil EMAT and rectangular spiral coil EMAT), all the factors in the conductor’s length direction (assumed to be the direction of the Z axis), including the difference of the field characteristics among the permanent magnet, coil, and specimen, can be neglected. So the EMAT can be simplified into a two-dimensional model on the coil’s cross section. Thus, among the field variables, the components of the x axis and y axis are the only factors that need to be considered.

2.2.1.1 The Weak Form of the Static Magnetic Field Equation of the Permanent Magnet

In the two-dimensional *Cartesian coordinate system*, the static magnetic field equation of the permanent magnet is expressed in (2.27).

$$\frac{\partial}{\partial x} \left(\mu \frac{\partial \varphi_m}{\partial x} \right) + \frac{\partial}{\partial y} \left(\mu \frac{\partial \varphi_m}{\partial y} \right) = 0 \quad (2.27)$$

The virtual displacement function $\delta \varphi_m$ is multiplied at both sides of the equation at the same time, and the integral is calculated to obtain (2.28).

$$\int_{\Omega} \left[\frac{\partial}{\partial x} \left(\mu \frac{\partial \varphi_m}{\partial x} \right) + \frac{\partial}{\partial y} \left(\mu \frac{\partial \varphi_m}{\partial y} \right) \right] \delta \varphi_m dA = 0 \quad (2.28)$$

In the above equation, Ω indicates the solution domain and dA indicates the surface element.

Carrying out partial integration for the left-hand side of the equation, we obtain (2.29).

$$\int_{\Omega} \mu \left(\frac{\partial \varphi_m}{\partial x} \frac{\partial \delta \varphi_m}{\partial x} + \frac{\partial \varphi_m}{\partial y} \frac{\partial \delta \varphi_m}{\partial y} \right) dA = \int_{\Gamma} \mu \frac{\partial \varphi_m}{\partial n} \delta \varphi_m dl \quad (2.29)$$

In the above equation, Γ indicates the boundary of the solution domain and dl is the boundary element.

2.2.1.2 The Weak Form of the Coil's Pulsed Eddy Current Field Equation

In the two-dimensional *Cartesian coordinate system*, the vector magnetic potential only has the component of the Z direction. The equation of the coil's pulsed eddy current field can be expressed in (2.30).

$$-\frac{\partial}{\partial x} \left(\frac{1}{\mu} \frac{\partial A_z}{\partial x} \right) - \frac{\partial}{\partial y} \left(\frac{1}{\mu} \frac{\partial A_z}{\partial y} \right) + \sigma \frac{\partial A_z}{\partial t} + \frac{1}{S} \iint_S \sigma \frac{\partial A_z}{\partial t} ds = J_{sz} \quad (2.30)$$

Multiplying the virtual displacement function δA_z of this equation and carrying out the integration is expressed by (2.31).

$$\begin{aligned} & \int_{\Omega} \left[-\frac{\partial}{\partial x} \left(\frac{1}{\mu} \frac{\partial A_z}{\partial x} \right) - \frac{\partial}{\partial y} \left(\frac{1}{\mu} \frac{\partial A_z}{\partial y} \right) + \sigma \frac{\partial A_z}{\partial t} + \frac{1}{S} \iint_S \sigma \frac{\partial A_z}{\partial t} ds \right] \delta A_z dA \\ &= \int_{\Omega} J_{sz} \delta A_z dA \end{aligned} \quad (2.31)$$

Carrying out partial integration for the above equation using Green's function as in (2.32).

$$\begin{aligned}
& \int_{\Omega} \left(\frac{1}{\mu} \frac{\partial A_z}{\partial x} \frac{\partial \delta A_z}{\partial x} + \frac{1}{\mu} \frac{\partial A_z}{\partial y} \frac{\partial \delta A_z}{\partial y} \right) dA \\
&= - \int_{\Omega} \sigma \frac{\partial A_z}{\partial t} \delta A dA + \int_{\Omega} \frac{1}{S} \iint_S \sigma \frac{\partial A_z}{\partial t} ds \delta A_z dA \\
&+ \int_{\Omega} J_{sz} \delta A_z dA + \int_{\Gamma} \frac{1}{\mu} \frac{\partial A_z}{\partial n} \delta A_z dl
\end{aligned} \tag{2.32}$$

2.2.1.3 The Weak Form of the Specimen's Wave Equation

The problem of the specimen's particle displacement caused by the *Lorentz force* can be simplified as a plane-strain problem in the elasticity mechanics. For the plane-strain problem, the desired characteristics of the geometry and external forces are listed as follows: The sample is very long along one direction and all of the cross sections that are perpendicular to this direction are the same; the conditions of displacement and support are also same; the surface traction and body force are both perpendicular to this direction and will not change with the length.

For the problem of a plane-strain condition, the direction of the length is supposed to be along the Z coordinate axis. Because the sample is very long, the sectional dimension and external force will not change with the length. The stress and strain also have no change along the Z coordinate axis. Thus, the factors to be concerned with are the stress, strain, and displacement components including ε_x , ε_y , ε_{xy} , σ_x , σ_y , σ_{xy} , u , and v .

In the two-dimensional *Cartesian coordinate system*, the equilibrium equations of each point along the direction of x and y in the specimen are expressed in (2.33) and (2.34).

$$\frac{\partial \sigma_x}{\partial x} + \frac{\partial \sigma_{xy}}{\partial y} + f_x = \rho \frac{\partial^2 u}{\partial t^2} \tag{2.33}$$

$$\frac{\partial \sigma_{xy}}{\partial x} + \frac{\partial \sigma_y}{\partial y} + f_y = \rho \frac{\partial^2 v}{\partial t^2} \tag{2.34}$$

The geometric equation is expressed in (2.35).

$$\varepsilon_x = \frac{\partial u}{\partial x}; \varepsilon_y = \frac{\partial v}{\partial y}; \varepsilon_{xy} = \frac{\partial u}{\partial y} + \frac{\partial v}{\partial x} \tag{2.35}$$

The physical equation is expressed in (2.36).

$$\left. \begin{aligned} \varepsilon_x &= \frac{1-\mu_p^2}{E} \left(\sigma_x - \frac{\mu_p}{1-\mu_p} \sigma_y \right) \\ \varepsilon_y &= \frac{1-\mu_p^2}{E} \left(\sigma_y - \frac{\mu_p}{1-\mu_p} \sigma_x \right) \\ \varepsilon_{xy} &= \frac{2(1+\mu_p)}{E} \sigma_{xy} \end{aligned} \right\} \quad (2.36)$$

In the above equation, E represents the material's elastic modulus and μ_p is the *Poisson* ratio.

For the equilibrium equation, the virtual displacement functions δu and δv were used to obtain (2.37).

$$\begin{aligned} & \int_{\Omega} \left[\left(\frac{\partial \sigma_x}{\partial x} + \frac{\partial \sigma_{xy}}{\partial y} + f_x \right) \delta u + \left(\frac{\partial \sigma_{xy}}{\partial x} + \frac{\partial \sigma_y}{\partial y} + f_y \right) \delta v \right] dA \\ &= \int_{\Omega} \left(\rho \frac{\partial^2 u}{\partial t^2} \delta u + \rho \frac{\partial^2 v}{\partial t^2} \delta v \right) dA \end{aligned} \quad (2.37)$$

Carrying out partial integration for the above equation and submitting it into the geometric equation as in (2.38).

$$\begin{aligned} & \int_{\Omega} (\sigma_x \delta \varepsilon_x + \sigma_y \delta \varepsilon_y + \sigma_{xy} \delta \varepsilon_{xy}) dV + \int_V \left(\rho \frac{\partial^2 u}{\partial t^2} \delta u + \rho \frac{\partial^2 v}{\partial t^2} \delta v \right) dA \\ &= \int_{\Omega} (f_x \delta u + f_y \delta v) dA + \int_{\Gamma} (T_x \delta u + T_y \delta v) dl \end{aligned} \quad (2.38)$$

In (2.38), T_x and T_y indicate the elastic sample's internal forces on the boundary. Because the specimen satisfies the boundary condition of traction free, the integral value on the right hand of the equation is zero.

2.2.2 The Weak Form of Coupled Equations in the Axisymmetric Coordinate System

For the spiral coil or EMAT used for the testing of the pipeline in the axial direction, the coil's structure and specimen satisfy the axisymmetric condition. In this case, the problem of three-dimensional analysis can be transformed into a two-dimensional problem in the axisymmetric coordinates. In the axisymmetric coordinates system, the vector magnetic potential and eddy current only have the component of θ direction and the other variables of various fields only have the components of r and z directions.

2.2.2.1 The Weak Form of the Permanent Magnet's Static Magnetic Field Equation

In the axisymmetric coordinates, the permanent magnet's static magnetic field equation is expressed in (2.39).

$$\frac{1}{r} \frac{\partial}{\partial r} \left(\mu r \frac{\partial \varphi_m}{\partial r} \right) + \frac{\partial}{\partial z} \left(\mu \frac{\partial \varphi_m}{\partial z} \right) = 0 \quad (2.39)$$

In this equation, the virtual displacement function $\delta \varphi_m$ is multiplied and the integral is calculated to obtain (2.40).

$$\int_{\Omega} \left[\frac{1}{r} \frac{\partial}{\partial r} \left(\mu r \frac{\partial \varphi_m}{\partial r} \right) + \frac{\partial}{\partial z} \left(\mu \frac{\partial \varphi_m}{\partial z} \right) \right] \delta \varphi_m dA = 0 \quad (2.40)$$

Using *Green's equation*, partial integration is carried out on the left part of the above equation as in (2.41).

$$\int_{\Omega} \mu \left(r \frac{\partial \varphi_m}{\partial r} \frac{\partial \delta \varphi_m}{\partial r} + r \frac{\partial \varphi_m}{\partial z} \frac{\partial \delta \varphi_m}{\partial z} \right) dA = \int_{\Gamma} \mu r \frac{\partial \varphi_m}{\partial n} \delta \varphi_m dl \quad (2.41)$$

2.2.2.2 The Weak Form of the Coil's Pulsed Eddy Current Field

Under the axisymmetric coordinates, the equation of the coil's pulsed eddy current field can be expressed by (2.42).

$$-\frac{\partial}{\partial r} \left(\frac{1}{r\mu} \frac{\partial A_{\theta}}{\partial r} \right) - \frac{\partial}{\partial z} \left(\frac{1}{\mu} \frac{\partial A_{\theta}}{\partial z} \right) + \sigma \frac{\partial A_{\theta}}{\partial t} + \frac{1}{S} \iint_s \sigma \frac{\partial A_{\theta}}{\partial t} ds = J_{s\theta} \quad (2.42)$$

Multiplying the virtual displacement function $\delta \varphi_m$ into the above equations, and carrying out the integration, (2.42) can be stated using (2.43).

$$\begin{aligned} & \int_{\Omega} \left[-\frac{\partial}{\partial r} \left(\frac{1}{r\mu} \frac{\partial A_{\theta}}{\partial r} \right) - \frac{\partial}{\partial z} \left(\frac{1}{\mu} \frac{\partial A_{\theta}}{\partial z} \right) + \sigma \frac{\partial A_{\theta}}{\partial t} + \frac{1}{S} \iint_s \sigma \frac{\partial A_{\theta}}{\partial t} ds \right] \delta A_{\theta} dA \\ &= \int_{\Omega} J_{s\theta} \delta A_{\theta} dA \end{aligned} \quad (2.43)$$

Using *Green's equation*, partial integration is carried out on the left part of the above equation, to obtain (2.44).

$$\begin{aligned}
\int_{\Omega} \frac{1}{\mu} \left(r \frac{\partial A_{\theta}}{\partial r} \frac{\partial \delta A_{\theta}}{\partial r} + r \frac{\partial A_{\theta}}{\partial z} \frac{\partial \delta A_{\theta}}{\partial z} \right) dA = & - \int_{\Omega} r \sigma \frac{\partial A_{\theta}}{\partial t} \delta A_{\theta} dA + \int_{\Omega} r J_{S\theta} \delta A_{\theta} dA \\
& + \int_{\Omega} r \frac{1}{S} \iint_S \sigma \frac{\partial A_{\theta}}{\partial t} ds \delta A_{\theta} dA + \int_{\Gamma} r \frac{1}{\mu} \frac{\partial A_{\theta}}{\partial n} \delta A_{\theta} dl
\end{aligned} \quad (2.44)$$

2.2.2.3 The Weak Form of the Specimen's Wave Equation

In the axisymmetric coordinate system, the deformation states are all the same in each radial plane of the object, that is, both of them have no relation with θ ; thus, the displacement components in the radial, tangential, and axial direction of each point in the object are expressed in (2.45).

$$u = u(r, z); v = 0; w = w(r, z) \quad (2.45)$$

In this way, the geometric equation satisfied by the elastic body is expressed in (2.46).

$$\varepsilon_r = \frac{\partial u}{\partial r}; \varepsilon_z = \frac{\partial u}{\partial z}; \varepsilon_{\theta} = \frac{u}{r}; \varepsilon_{rz} = \frac{\partial u}{\partial z} + \frac{\partial w}{\partial r} \quad (2.46)$$

According to the generalized *Hooke's law*, the stress-strain relationship can be expressed by (2.47), (2.48), (2.49), and (2.50).

$$\varepsilon_r = \frac{1}{E} [\sigma_r - \mu_p (\sigma_{\theta} + \sigma_z)] \quad (2.47)$$

$$\varepsilon_{\theta} = \frac{1}{E} [\sigma_{\theta} - \mu_p (\sigma_r + \sigma_z)] \quad (2.48)$$

$$\varepsilon_z = \frac{1}{E} [\sigma_z - \mu_p (\sigma_r + \sigma_{\theta})] \quad (2.49)$$

$$\varepsilon_{rz} = \frac{2(1 - \mu_p)}{E} \sigma_{rz} \quad (2.50)$$

In the above equations, σ_r , σ_{θ} , and σ_z represent the positive stress of each axis direction, respectively. σ_{rz} is the shear stress.

The equilibrium equations of particle motion are listed in (2.51) and (2.52).

$$\frac{\partial \sigma_r}{\partial r} + \frac{\partial \sigma_{rz}}{\partial z} + \frac{\sigma_r - \sigma_{\theta}}{r} + f_r = \rho \frac{\partial^2 u}{\partial t^2} \quad (2.51)$$

$$\frac{\partial \sigma_{rz}}{\partial r} + \frac{\partial \sigma_z}{\partial z} + \frac{\sigma_{rz}}{r} + f_z = \rho \frac{\partial^2 w}{\partial t^2} \quad (2.52)$$

In the above equations, f_r and f_z represent the body forces existing on the specimen and ρ represents the bulk density of the specimen.

The principle of virtual displacement is used on the equilibrium equation to get (2.53).

$$\begin{aligned} & \int_V \left[\left(\frac{\partial \sigma_{rr}}{\partial r} + \frac{\partial \sigma_{rz}}{\partial z} + \frac{\sigma_{rr} - \sigma_{\theta\theta}}{r} + f_r \right) \delta u + \left(\frac{\partial \sigma_{rz}}{\partial r} + \frac{\partial \sigma_{zz}}{\partial z} + \frac{\sigma_{rz}}{r} + f_z \right) \delta w \right] dV \\ &= \int_V \left(\rho \frac{\partial^2 u}{\partial t^2} \delta u + \rho \frac{\partial^2 w}{\partial t^2} \delta w \right) dV \end{aligned} \quad (2.53)$$

Partial integration is carried out on the above equation and the geometric equation is used to obtain (2.54).

$$\begin{aligned} & \int_V (\sigma_{rr} \delta \varepsilon_{rr} + \sigma_{zz} \delta \varepsilon_{zz} + \sigma_{rz} \delta \varepsilon_{rz}) dV + \int_V \left(\rho \frac{\partial^2 u}{\partial t^2} \delta u + \rho \frac{\partial^2 v}{\partial t^2} \delta v \right) \\ &= \int_V \left[\left(f_r + \frac{\sigma_{rr} - \sigma_{\theta\theta}}{r} \right) \delta u + \left(\frac{\sigma_{rz}}{r} + f_z \right) \delta v \right] dV + \int_{\Gamma} (T_r \delta u + T_z \delta v) d\Gamma \end{aligned} \quad (2.54)$$

In the above equation, T_r and T_z indicate the internal force of the specimen's boundary. Since the specimen satisfies the boundary conditions, both T_r and T_z are zero.

2.3 Finite Element Simulation of EMAT by COMSOL Multiphysics [2]

2.3.1 Simulation Procedure of EMAT by COMSOL Multiphysics

The *COMSOL Multiphysics* was used to do the modeling analysis of the problem described by the PDEs. There are two optional ways and one of them is the direct modeling for the PDEs. According to the expression form of the PDEs, it can be divided into three kinds: coefficient form, general form, and weak form. At the condition for which the parameters of the varied forms are given and their boundary conditions are satisfied, inputting those parameters and values of the boundary conditions means the modeling work of the physical model can be completed.

Another way is in using the analytical modules of the physical fields that are generally used, which are built into the *COMSOL Multiphysics*. Eight modules were included in the 3.5a edition of *COMSOL Multiphysics*, including AC/DC module, radio frequency module, acoustics module, chemical engineering module, geoscience module, heat transfer module, microelectromechanical system (MEMS) module, and structural mechanics module. No matter which module is selected, the essence of the finite element method using *COMSOL Multiphysics* is to solve the partial differential equations of the actual physical problems by transforming the equation set into the weak form with interface and boundary conditions. Therefore, the weak form is more widely used in carrying out the modeling work for the multiphysics coupling problem, for the reason that it is not only the clear essence of the FEM calculation of the multiphysics field, but also that it can be used to resolve the insoluble problem with the built-in module.

By using the *COMSOL Multiphysics*, the numerical methods and steps for the whole energy conversion process of EMAT based on the Lorentz force mechanism are listed as follows:

- (1) Selecting the coordinate system that needs to be solved. If the two-dimensional analysis is adopted, the 2D rectangular coordinate system or axisymmetric coordinate system can be selected. It is necessary to note that the 2D axisymmetric coordinate system does not support the modeling of the weak form by itself. In the process of weak form modeling, the coordinate system is transformed into a rectangular coordinate system.
- (2) The solving form was selected as the weak form. In this way, 4 set of equations should be selected.
- (3) Setting the geometric model of each component of EMAT. A solution domain should be given when the numerical simulation of the electromagnetic field is done. Thus, a solution domain should be defined beside the model.
- (4) According to those weak forms and boundary conditions of the various fields, the solution domain and boundary condition are set, respectively. For the EMAT based on the *Lorentz force* mechanism, besides the calculation of the coil's magnetic field when the skin effect and proximity effect are considered, the built-in modules of *COMSOL Multiphysics* can also be used in the calculation of the static magnetic field and mechanical field. Because the multifield coupling is involved, the coupling variable needs to be set. The product of the static magnetic induction intensity obtained from the solution of the static bias magnetic field, the specimen's magnetic permeability, and the particle's velocity is set as the density of the pulsed eddy current source when calculating the coil's ultrasonic wave. Because the induced electromotive force of each coil conductor should be calculated when calculating the ultrasonic signal received by the coils, the variables of the integral coupling should be set to calculate the induced electromotive force of each step length of the solution.
- (5) Meshing for the solution domain. In the process of meshing, two points are important in improving the accuracy of the calculation: One is that the

elements of the mesh should be more than 2 under the skin depth of the specimen's upper surface; and the other is guaranteeing that there are more than 7 elements of mesh within the wavelength of the excited ultrasonic wave inside the specimen.

- (6) Solving the model. The solution of the static bias magnetic field is a steady-state solution, while other fields are transient solutions. The transient solution needs to be set to the step length and the relative and absolute error of the solutions. Because the adoptive pulsed excitation signal is a tone-burst signal with high frequency, the step length should be set smaller to ensure the smoothness and stability of the solutions. Since the value of the displacement is small, the absolute error of the solution should be small enough during the process of solving the displacement of the internal points to ensure the correctness of the solution.
- (7) Postprocessing of the results, including the exhibition of the variables' surface plots of the various fields and transient waveforms.

2.3.2 Example of the Numerical Simulation and Experimental Verification

To verify the correctness of the derived mathematical model that is used to represent the EMAT's character and the effectiveness of the *COMSOL Multiphysics* based on the numerical simulation of EMAT's working process, an example of the modeling of EMAT was conducted and the calculation result was verified by experimental results.

2.3.2.1 The Parameters of the Simulation

The meander coil was used to excite *Lamb waves* within an aluminum plate. Because of the dispersive nature of *Lamb waves*, before the fabrication of the EMAT the phase velocity and group velocity dispersion curves of *Lamb waves* should be calculated based on the elastic modulus, *Poisson ratio*, and the thickness of the aluminum plate. The appropriate wave mode was selected according to the dispersion curves. The EMAT coil was designed based on the chosen point. The parameters of the aluminum plate are listed in Table 2.1.

Using the calculation software of the dispersion curves, the dispersion curves of phase velocity and group velocity for the *Lamb waves* in the aluminum plate under different frequency-thickness products are listed, respectively, as follows (Fig. 2.1):

The frequency-thickness product of the aluminum plate with a thickness of 3 mm was selected as $1100 \text{ m} \times \text{Hz}$. That is, the exciting frequency is 366.7 kHz. It is found that there are two modes of *Lamb waves* that can be generated at this condition: A_0 mode and S_0 mode. The phase velocity and group velocity of the A_0

Table 2.1 The dimension and parameters of the tested aluminum plate

Name	Value
Length	500 mm
Width	350 mm
Thickness	3 mm
Conductivity	3.5×10^7 S/m
Elasticity modulus	70 Gpa
Poisson ratio	0.33

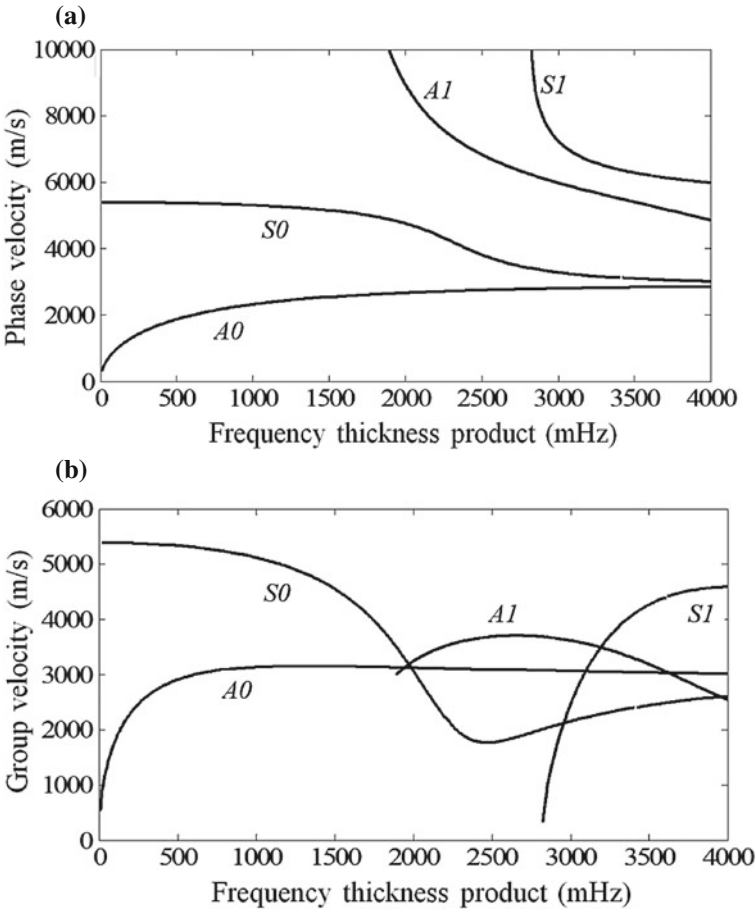


Fig. 2.1 The phase velocity (a) and group velocity (b) dispersion curves of Lamb waves in the aluminum plate

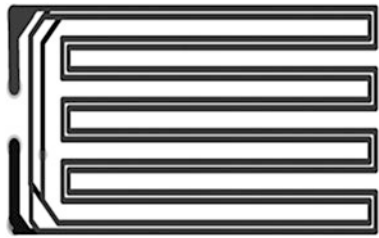


Fig. 2.2 The double-layer and double-split meander coil

Table 2.2 The coil’s dimensions and material’s parameters

Name	Value
Substrate thickness	0.500 mm
The width of the copper layer	0.720 mm
The thickness of the copper layer	0.035 mm
The line spacing	0.905 mm
The fold spacing	3.25 mm
The magnetic permeability of the copper layer	$4\pi \times 10^{-7}$ H/m
The electric conductivity of the copper layer	2.667×10^7 S/m

mode are 5287 and 5044 m/s, respectively. The adopted double-layer and double-split meander coil is shown in Fig. 2.2, with the distance between the adjacent folds being 6.5 mm (Table 2.2).

In the experiment, as shown in Fig. 2.3, excitation and receiving probes of EMAT were used for the excitation and receiving of ultrasonic waves. The excitation probe was installed 90 mm away from the left end of the aluminum plate, the receiving probe was installed 120 mm away from the left end, and the center-to-center spacing of the two probes was 140 mm. The liftoff distance between the two probe’s coil and the aluminum plate was 1 mm. A permanent magnet with a residual magnetic flux density of 1 T was located above the bending coil and the distance between them was 0.5 mm. The arrangement of the probe is shown in Fig. 2.3:

2.3.2.2 Experimental Setup

In order to verify the effectiveness of the simulation results, the pulse excitation and receiving device RPR-4000, produced by RITEC, was employed as the exciting source of the EMAT to produce the RF tone-burst signal. The amplitude and frequency of the signal can be adjusted arbitrarily to meet the requirements. Between the RPR-4000 and the excitation coil, an impedance matching device was used to complete the matching of the coil impedance and that of the exciting

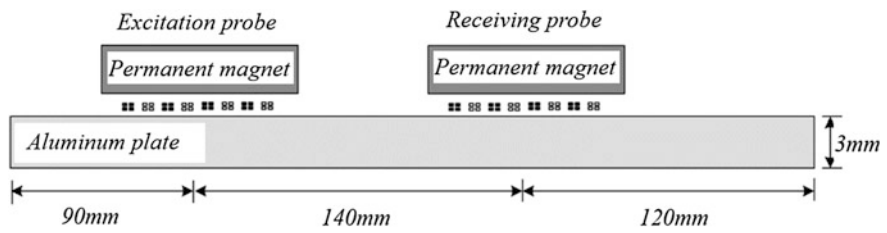


Fig. 2.3 A diagram of the arrangement of the probes for Lamb waves

source’s output. The filtering and amplification of the receiving signal can be achieved using the RPR-4000. The bandwidth and amplification factor of the filter are also adjustable. The matching of the coil impedance and the input impedance of the RPR-4000 is achieved by the connection of the receiving coil and the impedance matching device, so that a greater power output can be achieved. The signal received by the RPR-4000 was displayed on the oscilloscope and was processed by the data acquisition software *Wave Star for Oscilloscopes* to collect the data. The final waveform was displayed on the PC. The setup of the experimental system is shown in Fig. 2.4.

2.3.2.3 The Process and Result of Calculations

The waveform of the tone-burst current excitation signal with a frequency of 366.7 kHz and 5 cycles is shown in Fig. 2.5.

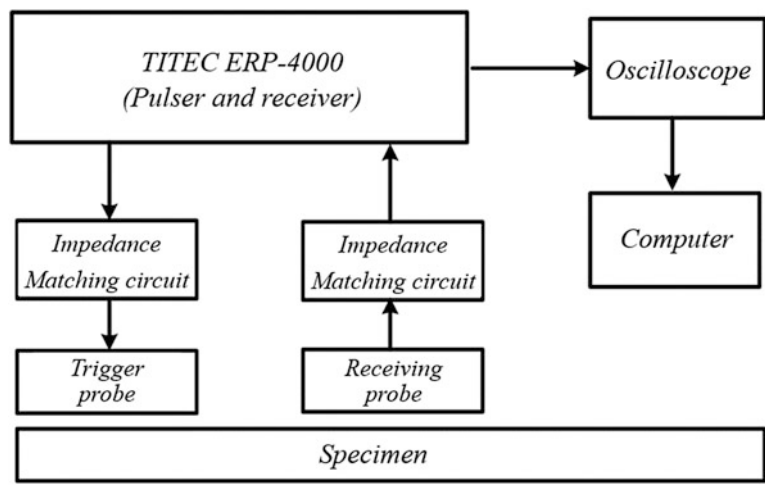
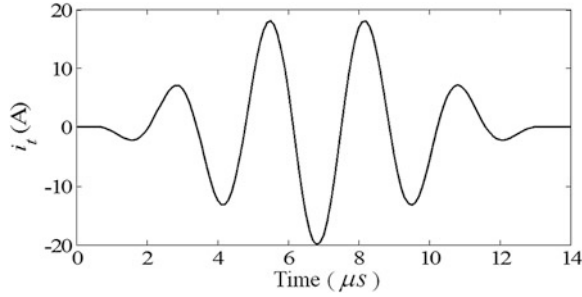


Fig. 2.4 The setup of the experimental system

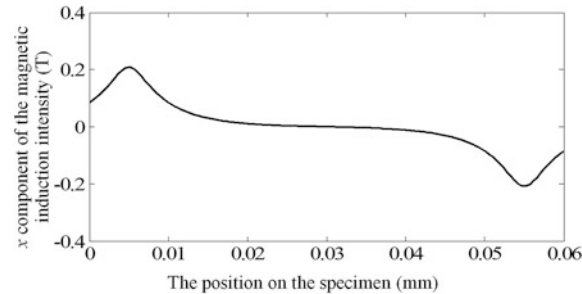
Fig. 2.5 The waveform of the excitation signal



The excitation current was input into *COMSOL Multiphysics* for simulation. The maximum element size in the meshing process inside the specimen was set as one-eighth of the wavelength of the *Lamb waves*, that is, 0.8125 mm. The time step is 0.00000002 s. In order to observe the obtained result, the observation points A and B inside the specimen were selected, with the location of point A just below the left-most conductor of the excitation coil, 0.01 mm below the top surface of the specimen under test. The location of point B is just below the center point of the receiving coil, 0.01 mm below the top surface of the specimen. A viewing zone C was selected, with its line segment located just below the exciting probe, 0.01 mm below the specimen's top face. Its width is 60 mm along the direction of the specimen's surface—the center of this line segment—in the horizontal coordinate, corresponding to the center of the meander coil and the permanent magnet.

Figures 2.6 and 2.7 show the *x* and *y* components of the static magnetic induction intensity generated by the permanent magnet in area C. In Fig. 2.6, the *x* components of the magnetic induction intensity are distributed symmetrically along the center of the area, with the values increasing from the center to both sides. The maximum value is located at the edge of the magnet. In Fig. 2.7, the *y* components of the magnetic induction intensity have a saddle-type distribution across the region. It is approximately a constant in the center of the area, with the values increasing from the center to both sides. The maximum value is also located at the edge of the magnet. It is found that, when the permanent magnet is reasonably well

Fig. 2.6 The *x* component of the static magnetic induction intensity



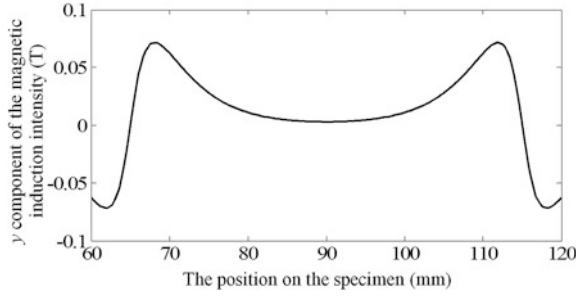


Fig. 2.7 The y component of the static magnetic induction intensity

designed, the y component of the bias magnetic field within the coil's area can be taken as a constant.

Figure 2.8 shows the equipotential line plot of the vector magnetic potential generated by the meander coil at a time of $10\ \mu\text{s}$ when the tone burst is applied on the coil. With the pulsed magnetic field, the coil's induced eddy current and its distribution within the skin depth of the specimen's top surface are shown in Figs. 2.9 and 2.10. It is illustrated that, since the current direction of the two adjacent wires of the meander coil is opposite to each other, the direction of the induced eddy current inside the specimen is also opposite, below the meander coil, and the values of the eddy current density below each of the coil's line segments are approximately equal. The bias magnetic field, as shown in Figs. 2.6 and 2.7, which is affected by the pulsed eddy current, as shown in Fig. 2.10, can be used to generate *Lorentz force* inside the specimen. The force will be applied to the internal point of the specimen. At the moment of $10\ \mu\text{s}$, the distributions of *Lorentz force* in area C are shown in Figs. 2.11 and 2.12. Figure 2.11 shows the x component of the *Lorentz force* and Fig. 2.12 shows the y component of the *Lorentz force*. It is shown that, even if the densities of the eddy currents below each bending section of the

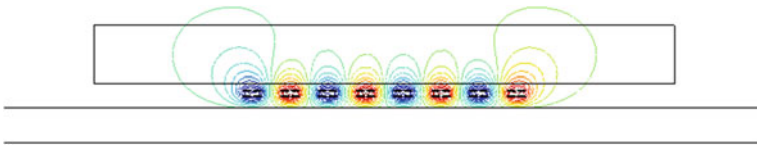


Fig. 2.8 The equipotential line of the vector magnetic potential

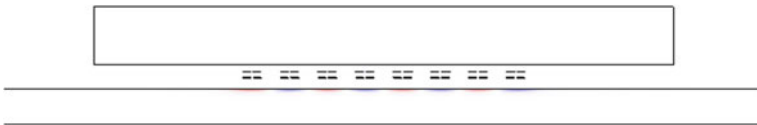


Fig. 2.9 The eddy current distribution inside the specimen at a time of $10\ \mu\text{s}$

Fig. 2.10 The eddy current distribution on area *C* at a time of 10 μ s

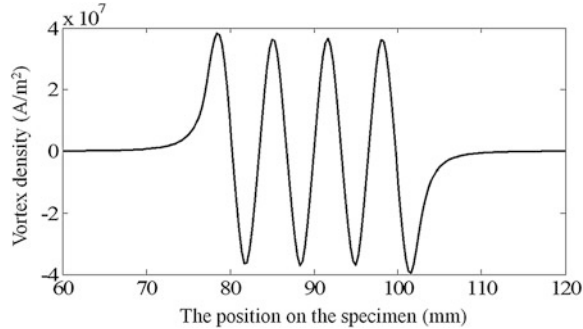


Fig. 2.11 The *x* component of Lorentz force on area *C* at a time of 10 μ s

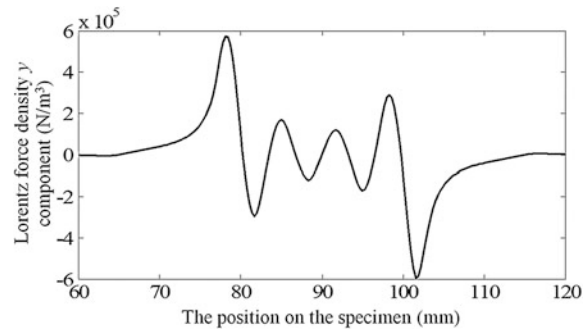
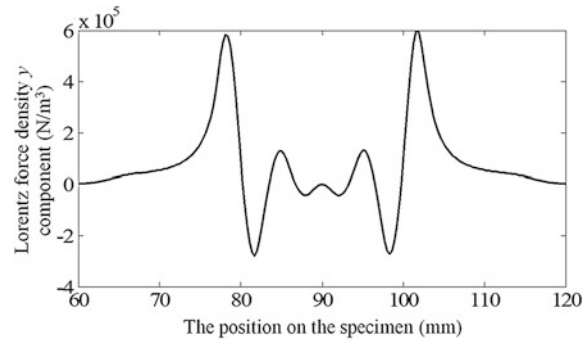
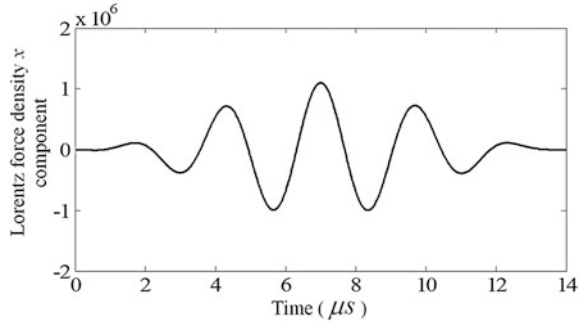


Fig. 2.12 The *y* component of Lorentz force on area *C* at the time of 10 μ s



coil are equal to each other, there is a big difference in the *Lorentz force* inside the specimen below each fold line of the coil for the reason that the force is generated under the bias magnetic field with a non-uniform distribution. Therefore, if the magnet is poorly designed, the approximate average area of the magnetic field generated by the magnet will be smaller than the coil's width. It will bring a large calculation error with the assumption that the bias magnetic field is of uniform distribution.

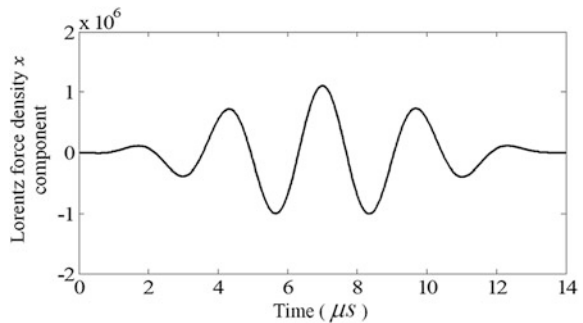
Fig. 2.13 The temporal variation of the *Lorentz force's* x component at point A



Figures 2.13 and 2.14 show the characteristics of a temporal variation of the *Lorentz force's* components x and y at the viewpoint A. Under the effect of the pulsed eddy current and bias magnetic field, the duration of the *Lorentz force* generated inside the specimen and that of the pulse are the same. The particles inside the specimen will generate vibration, exciting the ultrasonic wave, and the ultrasonic waves will propagate along the aluminum plate to be tested.

Figure 2.15 shows the x component of the internal particle's displacement of the specimen at the moment of 0, 10, 30, and 50 μs . It shows the process of the ultrasonic wave propagation in the specimen. At the moment of 0 μs , the excitation is still not applied on the coil, and there is no ultrasonic wave generated; at the time of 10 μs , the ultrasonic wave has been already generated, and it begins to propagate in two different directions; at the moment of 30 μs , the coil's excitation has already completed and the ultrasonic wave continues to propagate in two different directions. At this moment, two kinds of ultrasonic wave (A_0 and S_0) are excited inside the specimen. At the moment of 50 μs , the ultrasonic wave of the S_0 mode that propagates to the right side has already passed the receiving probe, while the ultrasonic wave of the A_0 mode has also arrived at the receiving probe. Meanwhile, the ultrasonic waves of the A_0 and S_0 mode, which propagate to the left side at first, are reflected from the left end of the specimen and change their direction of propagation to the right side of the specimen.

Fig. 2.14 The temporal variation curve of the *Lorentz force's* y component at point A



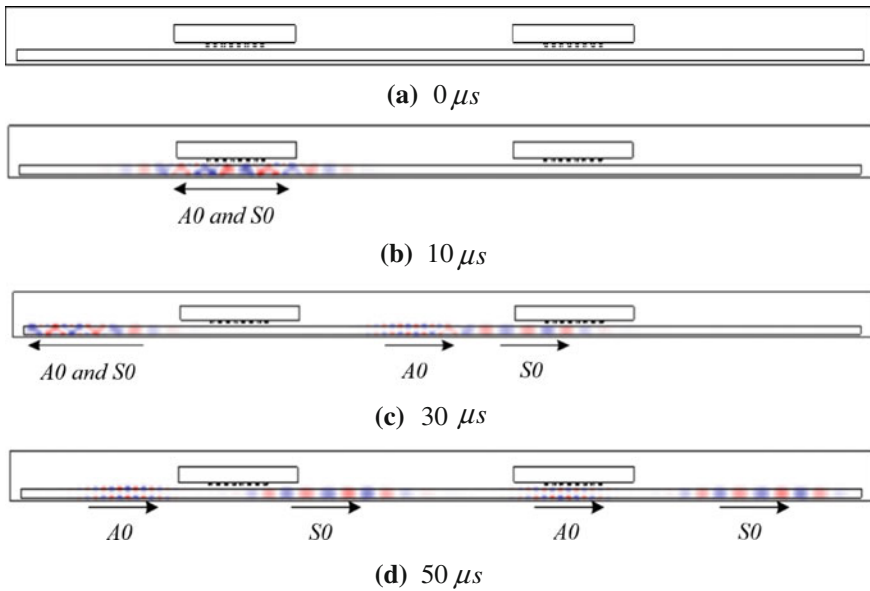


Fig. 2.15 The temporal variation of particle displacement component x

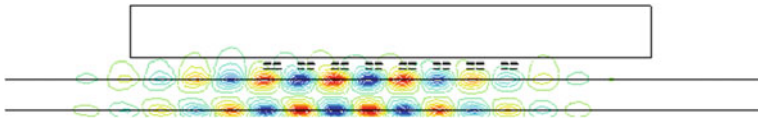


Fig. 2.16 The equipotential line of the magnetic vector potential generated by the particle motion inside the specimen

When the ultrasonic waves propagate to the receiving probe, the particle motion inside the specimen will generate a dynamic magnetic field under the effect of the bias magnetic field. An induced electromotive force will be generated inside the receiving coil, thus realizing the signal reception. At the moment of $50 \mu s$, the equipotential lines of the magnetic vector potential are generated by the particle motion inside the specimen, as shown in Fig. 2.16.

Figure 2.17 shows the normalized waveform of the receiving signal from the receiving coil within $120 \mu s$ after the excitation from the probe. As illustrated in Fig. 2.17, the receiving probe receives 5 wave packets within the first $120 \mu s$. For convenience, in the analysis each wave packet is named separately as S_{0R} , A_{0R} , S_{0LR} , S_{0L} , and A_{0LR} , according to the ultrasonic mode and the direction of their propagation. S_{0R} is the *Lamb wave* of the S_0 mode that propagates to the right side in the earliest stage; A_{0R} is the *Lamb wave* of the A_0 mode that propagates to the right side in the earliest stage; S_{0LR} represents the *Lamb wave* of the S_0 mode that propagates to the right side in the earliest stage and then propagates to the left side after the reflection at

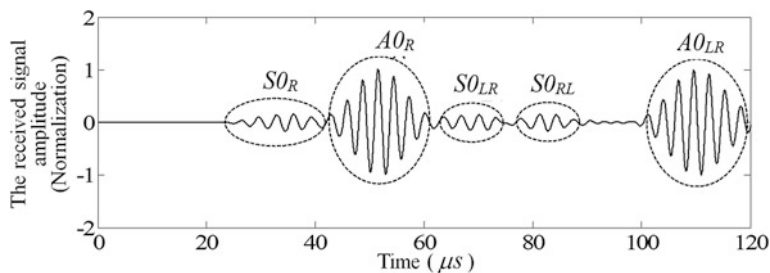


Fig. 2.17 The induced electromotive force of the receiving coil

the right end of the specimen; S_{0RL} represents the *Lamb wave* of the S_0 mode that propagates to the left side in the earliest stage and then propagates to the right side after the reflection at the left end of the specimen; and A_{0LR} is the *Lamb wave* of the A_0 mode that propagates to the left side in the earliest stage and then propagates to the right side after the reflection at the left end of the specimen.

In the experiment, the parameters used for EMAT are the same as those of the computational model, and the impulse excitation of the same frequency and number of periods is applied in the experiment. The normalized waveform of the received signal from the receiving probe in the experiment is shown in Fig. 2.18. Comparing Fig. 2.17 with 2.18, it can be found that the corresponding time of either the ultrasonic waves or of the wave packet received in the experiment is relatively comparable with that of the simulation results. This verifies the correctness and effectiveness of the numerical simulation method of the whole energy conversion process of the *Lorentz force*-based EMAT discussed in this book.

Based on the ultrasonic wave propagation distance for a certain time period, the group velocities of the *Lamb wave* of the S_0 mode and A_0 mode obtained from the numerical simulation and experiment can be calculated. A comparison of these values with the theoretical values is given in Table 2.3.

Table 2.3 shows that the differences among the theoretical, simulation, and experimental values of wave velocity are negligible and so proves the correctness and effectiveness of the simulation results and the experimental results.

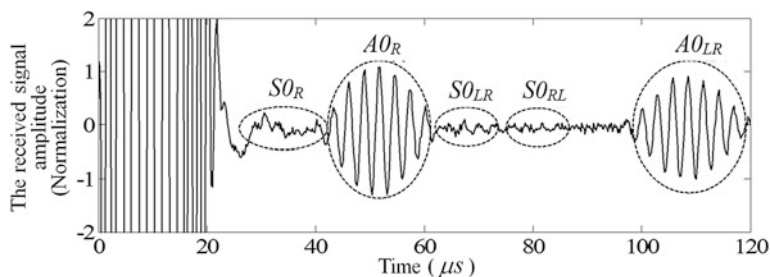


Fig. 2.18 The measured results from the receiving probe

Table 2.3 The comparisons of wave velocities

Wave mode	Theoretical wave velocity (m/s)	Simulation wave velocity (m/s)	Experimental wave velocity (m/s)
S_0	3148	3102	3147
A_0	5044	5291	5263

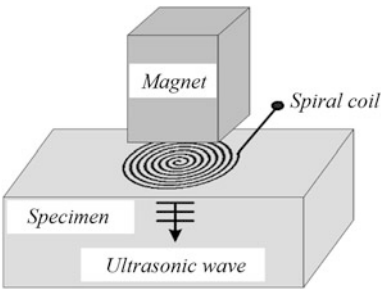
2.4 Analytical Modeling and Calculation of EMAT with Spiral Coil [3]

2.4.1 Configurations of the EMAT with Spiral Coils

Spiral coils can be used to excite and receive ultrasonic bulk waves inside the specimen. The typical configuration of the bulk wave EMAT is shown in Fig. 2.19. The permanent magnet or electromagnet is used to provide a static bias magnetic field which is perpendicular to the spiral coil and specimen. The spiral coil is placed above the specimen. When the spiral coil is supplied by the pulsed excitation with the desired center frequency, the ultrasonic wave could be generated by *Lorentz force* or magnetostrictive effect and propagates perpendicularly to the surface of the specimens. The echo wave could be detected in terms of the inverse process of generation.

In practical applications, the spiral coils are made by a printed circuit board (PCB) or flexible plate (FPC) technique for accurate design of the dimensions, compact configuration, and convenient application. The coil could be designed with single-layer or double-layer configurations, which consist of rectangular spiral copper wires on a fiberglass substrate. The sectional view schematic diagrams of the coils are shown in Figs. 2.20 and 2.21.

Fig. 2.19 The structure of EMAT: permanent magnet, spiral coil, and specimen



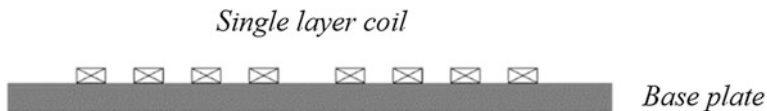


Fig. 2.20 The single-layer planar spiral coil

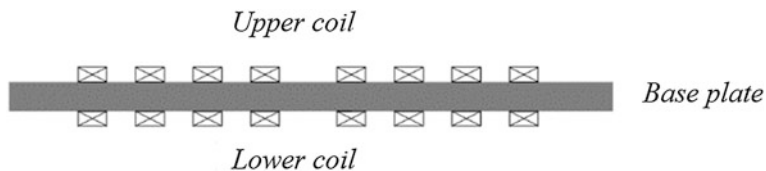


Fig. 2.21 The double-layer planar spiral coil

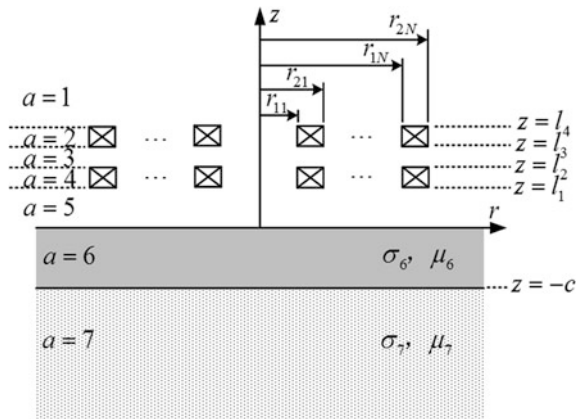
2.4.2 Frequency-Domain Solution

To analytically express the solutions, the following derivations and calculations are based on some assumptions:

- (1) The mediums in all solution domains are linear, isotropic, and homogeneous.
- (2) The proximity effect and skin effect for the copper wires are neglected, i.e., the distribution of current density is uniform in the copper wires.
- (3) The displacement current is neglected because of its small value.
- (4) The spiral coils are viewed as a superposition of concentric circles carrying the same current.

For the frequency-domain calculation of the magnetic field, the cylindrical coordinate system is used to model the EMAT. Thus, the magnetic vector potential (MVP) in each solution domain only has circumferential components. The physical model of the EMAT with a double-layer spiral coil in the cylindrical coordinates is illustrated in Fig. 2.22. The spiral coil is viewed as the arrays of N -concentric copper wire circles. The radiuses of the circles are as follows: $r_{11}, r_{21}, r_{12}, r_{22}, \dots, r_{1N}, r_{2N}$. The dimensions of the spiral coil in the z direction are l_1, l_2, l_3 , and l_4 . The thickness of the specimen is c . A conducting half-space is below the specimen. When the spiral coil is a single layer, the model can be simplified by deleting the terms containing l_3 and l_4 in the analytical expression. Seven solution domains are partitioned along the z direction and indicated as $a = 1, 2, \dots, 7$, for calculation. Because the substrate of the coil has the same permeability and conductivity as air, we view it as air in the derivation process. The conductive specimens are non-magnetic.

Fig. 2.22 Double-layer spiral coil at a distance above a conductive specimen and an infinite half-space

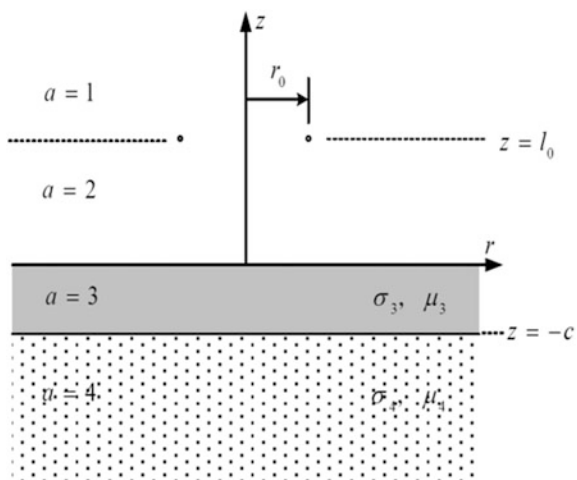


2.4.2.1 The Magnetic Vector Potential of a Delta Function Coil

To begin with, the MVP of a delta function coil $\delta(r - r_0)\delta(z - z_0)$ above a specimen is calculated. The schematic diagram is shown in Fig. 2.23, in which four solution domains are partitioned. The frequency-domain differential equation of the delta function coil above the specimen can be expressed as shown in (2.55); the solution area is 4.

$$\left(\frac{\partial^2}{\partial r^2} + \frac{1}{r} \frac{\partial}{\partial r} + \frac{\partial^2}{\partial z^2} - \frac{1}{r^2} - j\omega\mu_a\sigma_a \right) A_a(\omega, r, z) = -\mu_a i(\omega) \delta(r - r_0) \delta(z - z_0) \quad (2.55)$$

Fig. 2.23 Delta function coil at (r_0, z_0) above a conductive specimen and an infinite half-space



In the above equation, $A_a(\omega, r, z)$ is the MVP; $i(\omega)$ is the excitation current density; μ_a and σ_a are the permeability and conductivity, respectively, and $a = 1, 2, 3, 4$ represent the solution domains.

At the boundaries between adjacent domains, the boundary conditions as shown in (2.56) should be satisfied.

$$A_a(\omega, r, z_a) = A_{a+1}(\omega, r, z_a) \quad (2.56)$$

$$\left. \frac{1}{\mu_a} \frac{\partial A_a}{\partial z} \right|_{z=z_a} = \left. \frac{1}{\mu_{a+1}} \frac{\partial A_{a+1}}{\partial z} \right|_{z=z_a} - i(\omega) \delta(r - r_0) \delta(z - z_0) \quad (2.57)$$

The solutions in each domain can be obtained by the method of separation of variables, and they can be expressed by (2.58), (2.59), (2.60), and (2.61).

$$A_1(r, z) = \frac{1}{2} \mu_0 i(\omega) r_0 \int_0^\infty J_1(kr_0) J_1(kr) e^{-kl-kz} (e^{2kl} + P_1) dk \quad (2.58)$$

$$A_2(r, z) = \frac{1}{2} \mu_0 i(\omega) r_0 \int_0^\infty J_1(kr_0) J_1(kr) e^{-kl} (e^{kz} + P_1 e^{-kz}) dk \quad (2.59)$$

$$A_3(r, z) = \mu_0 i(\omega) r_0 \int_0^\infty J_1(kr_0) J_1(kr) e^{-kl} (P_2 e^{K_3 z} + P_3 e^{-K_3 z}) dk \quad (2.60)$$

$$A_4(r, z) = \mu_0 i(\omega) r_0 \int_0^\infty J_1(kr_0) J_1(kr) e^{-kl} P_4 e^{-K_4 z} dk \quad (2.61)$$

In the above equations, $J_1(x)$ is the first kind and first order of the *Bessel function*. Other related parameters can be expressed as follows:

$$\begin{aligned} K_a &= \sqrt{k^2 + j\omega\mu_a\sigma_a} \\ P_1 &= \frac{(k + K_3)(K_3 - K_4) + (k - K_3)(K_4 + K_3)e^{2K_3e}}{(k - K_3)(K_3 - K_4) + (k + K_3)(K_4 + K_3)e^{2K_3e}} \\ P_2 &= \frac{k(K_3 + K_4)e^{2K_3e}}{(k - K_3)(K_3 - K_4) + (k + K_3)(K_4 + K_3)e^{2K_3e}} \\ P_3 &= \frac{k(K_3 - K_4)}{(k - K_3)(K_3 - K_4) + (k + K_3)(K_4 + K_3)e^{2K_3e}} \\ P_4 &= \frac{2K_3ke^{(K_3 + K_4)e}}{(k - K_3)(K_3 - K_4) + (k + K_3)(K_4 + K_3)e^{2K_3e}} \end{aligned}$$

2.4.2.2 The MVP of the Spiral Coil

For the rectangular section planar spiral coil, we choose one circle to consider first. Then, the overall MVP can be calculated by the superposition theorem. As far as the circles with the radiuses r_{11} , r_{12} and heights l_1 , l_2 are concerned, the MVP in each solution domain is the superposition of those of the delta function coils and can be calculated by (2.62).

$$A_a(\omega, r, z) = \int_S A_a(\omega, r, z, r_0, l_0) ds = \int_{r_1}^{r_2} \int_{l_1}^{l_2} A_a(\omega, r, z, r_0, l_0) dr_0 dl \quad (2.62)$$

In the above equation, $A_a(\omega, r, z)$ is the MVP of the delta function coil positioned at (r_0, l_0) .

The integration is performed and the MVP of the chosen circle is expressed in (2.63), (2.64), (2.65), and (2.66).

$$A_{1,2,3}^c(\omega, r, z) = \frac{1}{2} \mu_0 i(\omega) \int_0^\infty \frac{1}{k^3} I(kr_1, kr_2) J_1(kr) e^{-kz} [e^{kl_2} - e^{kl_1} - P_1(e^{-kl_2} - e^{-kl_1})] dk \quad (2.63)$$

$$A_5^c(\omega, r, z) = \frac{1}{2} \mu_0 i(\omega) \int_0^\infty \frac{1}{k^3} I(kr_1, kr_2) J_1(kr) [(e^{-kl_1} - e^{kl_2})(e^{kz} + P_1 e^{-kz})] dk \quad (2.64)$$

$$A_6^c(\omega, r, z) = \mu_0 i(\omega) \int_0^\infty \frac{1}{k^3} I(kr_1, kr_2) J_1(kr) [(e^{-kl_1} - e^{kl_2})(P_2 e^{K_1 z} + P_3 e^{-K_1 z})] dk \quad (2.65)$$

$$A_7^c(\omega, r, z) = \mu_0 i(\omega) \int_0^\infty \frac{1}{k^3} J(kr_1, kr_2) J_1(kr) (e^{-kl_1} - e^{-kl_2}) P_4 e^{K_2 z} dk \quad (2.66)$$

In the above equations, the superscript c represents the MVP of the chosen circle and K_6 and K_7 take the place of K_3 and K_4 in P_1 , P_2 , P_3 , and P_4 .

$$\begin{aligned}
I(x_1, x_2) &= \int_{x_1}^{x_2} x J_1(x) dx \\
&= \frac{\pi}{2} \{x_2 [J_0(x_2) H_1(x_2) - J_1(x_2) H_0(x_2)] \\
&\quad - x_1 [J_0(x_1) H_1(x_1) - J_1(x_1) H_0(x_1)]\}
\end{aligned} \tag{2.67}$$

In (2.67), H_n represents the Struve function.

(2.65) and (2.65) are valid for the domains above the coil and below the coil, respectively. The MVP in domain 4 can be obtained by substituting $l_1 = z$ in (2.64), and adding (2.68).

$$\begin{aligned}
A_4^c(\omega, r, z) \\
= \frac{1}{2} \mu_0 i(\omega) \int_0^\infty \frac{1}{k^3} I(kr_1, kr_2) J_1(kr) \left[2 - e^{k(z-l_2)} - e^{-k(z-l_1)} + P_1(e^{-kl_1} - e^{-kl_2})e^{-kz} \right] dk
\end{aligned} \tag{2.68}$$

On the basis of the MVP of a single coil, the MVP of other $n - 1$ circles in the lower-layer coil could be obtained in the same way. We add all the MVPs of each circle to obtain the MVP of all the lower-layer coils, as shown in (2.69).

$$A_a^l(\omega, r, z) = \sum_i^N A_a^{lci}(\omega, r, z) \tag{2.69}$$

In the above equation, the superscript l represents the lower-layer coil. In the same way, replacing l_1 and l_2 with l_3 and l_4 , we get the MVP of the upper-layer coil, as shown in (2.70).

$$A_a^u(\omega, r, z) = \sum_i^N A_a^{uci}(\omega, r, z) \tag{2.70}$$

In the above equation, the superscript u represents the upper-layer coil. Thus, the MVP of the double-layer spiral coil is expressed in (2.71).

$$A_a^d(\omega, r, z) = A_a^l(\omega, r, z) + A_a^u(\omega, r, z) \tag{2.71}$$

In the above equation, the superscript d represents the double-layer coil. Here, what we are concerned with are the MVPs in domains 2, 4, and 6 in Fig. 2.22. They are derived in (2.72).

$$\begin{aligned}
& A_6^d(\omega, r, z) \\
& = \mu_0 i(\omega) \int_0^\infty \frac{1}{k^3} \sum_i^N I(kr_{1i}, kr_{2i}) J_1(kr) (e^{-kl_1} - e^{-kl_2} + e^{-kl_3} - e^{-kl_4}) (P_2 e^{K_1 z} + P_3 e^{-K_1 z}) dk
\end{aligned} \tag{2.72}$$

$$\begin{aligned}
& A_2^d(\omega, r, z) = \frac{1}{2} \mu_0 i(\omega) \int_0^\infty \frac{1}{k^3} \sum_i^N I(kr_{1i}, kr_{2i}) J_1(kr) \\
& \left[2 - e^{k(z-l_4)} - e^{-k(z-l_3)} + e^{-k(z-l_2)} - e^{-k(z-l_1)} + P_1 (e^{-kl_1} - e^{-kl_2} + e^{-kl_3} - e^{-kl_4}) e^{-kz} \right] dk
\end{aligned} \tag{2.73}$$

$$\begin{aligned}
& A_4^d(\omega, r, z) = \frac{1}{2} \mu_0 i(\omega) \int_0^\infty \frac{1}{k^3} \sum_i^N I(kr_{1i}, kr_{2i}) J_1(kr) \\
& \left[2 - e^{k(z-l_2)} - e^{-k(z-l_1)} + e^{-k(z-l_3)} - e^{-k(z-l_4)} + P_1 (e^{-kl_1} - e^{-kl_2} + e^{-kl_3} - e^{-kl_4}) e^{-kz} \right] dk
\end{aligned} \tag{2.74}$$

2.4.2.3 Analytical Expression of Magnetic Flux Intensity, Pulsed Eddy Current and Input Impedance

The dynamic magnetic flux density in the specimen can be calculated according to (2.75).

$$B = \nabla \times A \tag{2.75}$$

Because A only has the component φ , B will only have the r component and z component.

$$\begin{aligned}
& B_r(\omega, r, z) = \\
& - \mu_0 i(\omega) \int_0^\infty \frac{1}{k^3} \sum_i^N I(kr_{1i}, kr_{2i}) J_1(kr) (e^{-kl_1} - e^{-kl_2} + e^{-kl_3} - e^{-kl_4}) (P_2 K_1 e^{K_1 z} - P_3 K_1 e^{-K_1 z}) dk
\end{aligned} \tag{2.76}$$

$$\begin{aligned}
& B_z(\omega, r, z) = \\
& \mu_0 i(\omega) \int_0^\infty \frac{1}{k^2} \sum_i^N I(kr_{1i}, kr_{2i}) J_0(kr) (e^{-kl_1} - e^{-kl_2} + e^{-kl_3} - e^{-kl_4}) (P_2 e^{K_1 z} + P_3 e^{-K_1 z}) dk
\end{aligned} \tag{2.77}$$

The pulsed eddy current is induced in the skin depth of the specimen. In terms of the relationship between the eddy current J and the MVP in the frequency domain, i.e., $\mathbf{J} = -j\omega\sigma\mathbf{A}$, the pulsed eddy current can be obtained by substituting (2.72).

$$J(\omega, r, z) = -j\omega\sigma_6\mu_0i(\omega) \int_0^\infty \frac{1}{k^3} \sum_i^N I(kr_{1i}, kr_{2i}) J_1(kr) (e^{-kl_1} - e^{-kl_2} + e^{-kl_3} - e^{-kl_4}) (P_2 e^{K_1 z} + P_3 e^{-K_1 z}) dk \quad (2.78)$$

Before calculating the input impedance, the induced voltage should be obtained first. The induced voltage in the rectangular cross-sectional circle coil is expressed in (2.79).

$$V(\omega) = \frac{j\omega 2\pi}{\text{coilcross section}} \iint_{\text{coilcrosssection}} rA(\omega, r, z) \quad (2.79)$$

The induced voltage of the double-layer coil is obtained by adding all the circles and can be expressed by (2.80).

$$V^d(\omega) = \sum_i^N \left[\frac{j\omega 2\pi}{(l_2 - l_1)(r_{2i} - r_{1i})} \int_{l_1}^{l_2} \int_{r_{1i}}^{r_{2i}} rA_2^d(\omega, r, z) dr dz + \frac{j\omega 2\pi}{(l_4 - l_3)(r_{2i} - r_{1i})} \int_{l_3}^{l_4} \int_{r_{1i}}^{r_{2i}} rA_4^d(\omega, r, z) dr dz \right] \quad (2.80)$$

Substituting (2.73) and (2.74) into (2.80) and adding the direct current resistance of the coil, the expression of the coil's input impedance in terms of *Ohm's law* can be obtained.

$$\begin{aligned} Z(\omega) = & Z_0 + \sum_{i=1}^N \left\{ \frac{j\omega\mu_0 2\pi}{(l_2 - l_1)^2 (r_{2i} - r_{1i})^2} \int_0^\infty \frac{1}{k^6} I(kr_{1i}, kr_{2i}) \sum_{i=1}^N I(r_{1i}, r_{2i}) \sum_{i=1}^N I(r_{1i}, r_{2i}) \right. \\ & [2k(l_2 - l_1) + 2(e^{-k(l_2 - l_1)} - 1) + (e^{-kl_1} - e^{-kl_2})(e^{kl_4} - e^{kl_3}) \\ & + P_1(e^{-kl_1} - e^{-kl_2} + e^{-kl_3} - e^{-kl_4})(e^{-kl_1} - e^{-kl_2})] dk \\ & + \frac{j\omega\mu_0 2\pi}{(l_4 - l_3)^2 (r_{2i} - r_{1i})^2} \int_0^\infty \frac{1}{k^6} I(r_{1i}, r_{2i}) \sum_{i=1}^N I(r_{1i}, r_{2i}) \\ & [2k(l_4 - l_3) + 2(e^{-k(l_4 - l_3)} - 1) + (e^{-kl_1} - e^{-kl_2})(e^{kl_4} - e^{kl_3}) \\ & \left. + P_1(e^{-kl_3} - e^{-kl_4} + e^{-kl_1} - e^{-kl_2})(e^{-kl_3} - e^{-kl_4})] dk \right\} \quad (2.81) \end{aligned}$$

In the above equation, Z_0 is the direct current resistance of the coil.

$$Z_0 = \frac{1}{\sigma_6} \sum_{i=1}^N \left[\frac{\pi(r_{2i} + r_{1i})}{(r_{2i} - r_{1i})(l_2 - l_1)} + \frac{\pi(r_{2i} + r_{1i})}{(r_{2i} - r_{1i})(l_4 - l_3)} \right] \quad (2.82)$$

2.4.2.4 Series Expressions of Flux Density, Eddy Current, and Input Impedance

In the expression of magnetic flux density, pulsed eddy current, and input impedance, the infinite integration is difficult to implement because the integrand is too complicated and contains double integrals of the one-order Bessel function. To lower the calculation difficulty, the approximate series expression of the magnetic flux density, pulsed eddy current, and input impedance is proposed by the truncated-domain eigenfunction expansion (TREE) method. Although the number of series terms and truncated distances bring about calculation errors, the errors can be readily controlled.

By setting the solution area as $0 \leq r \leq \infty$ instead of $0 \leq r \leq R$, the infinite integration can be transformed into the sum of an infinite series. When the chosen R is large enough, the calculation results will be consistent with the real results. According to the physical significance of MVP, it is bounded in the solution area and a magnetic insulation boundary condition is exerted.

$$|A|_{r < R} < \infty \quad (2.83)$$

$$A|_{r < R} = 0 \quad (2.84)$$

Then, the general solution of MVP can be expressed by (2.85).

$$A_n(\omega, r, z) = \sum_{m=1}^{\infty} (A_m(k_m)e^{K_n z} + B_m(k_m)e^{-K_n z})C_m(k_m)J_1(k_m r) \quad (2.85)$$

According to (2.84), we can get (2.86).

$$J_1(k_m R) = 0 \quad (2.86)$$

It is found that $K_m R$ is the m th zero root x_m of $J_1(x)$. Thus, (2.87) can be obtained.

$$k_m = \frac{x_m}{R} \quad (2.87)$$

After a series of derivations, in a similar manner to the above sections, the ultimate series expressions of magnetic flux density, pulsed eddy current, and input impedance are expressed by (2.88), (2.89), (2.90), and (2.91).

$$B_r = -2\mu_0 i(\omega) \sum_{i=1}^N \sum_{m=1}^{\infty} \frac{I(kr_{1i}, kr_{2i}) J_1(k_m r)}{k_m^4 R^2 J_0^2(k_m R)} \quad (2.88)$$

$$(e^{-k_m l_1} - e^{-k_m l_2} + e^{-k_m l_3} - e^{-k_m l_4}) (P_{2m} K_{1m} e^{K_{1m} z} - P_{3m} K_{1m} e^{-K_{1m} z})$$

$$B_z(\omega, r, z) = 2\mu_0 i(\omega) \sum_{i=1}^N \sum_{m=1}^{\infty} \frac{I(kr_{1i}, kr_{2i}) J_0(k_m r)}{k_m^3 R^2 J_0^2(k_m R)} \quad (2.89)$$

$$(e^{-kl_1} - e^{-kl_2} + e^{-kl_3} - e^{-kl_4}) (P_{2m} e^{K_{1m} z} + P_{3m} e^{-K_{1m} z})$$

$$J_e(\omega, r, z) = -2j\omega\sigma_6\mu_0 i(\omega) \sum_{i=1}^N \sum_{m=1}^{\infty} \frac{I(kr_{1i}, kr_{2i}) J_0(k_m r)}{k_m^4 R^2 J_0^2(k_m R)} \quad (2.90)$$

$$(e^{-k_m l_1} - e^{-k_m l_2} + e^{-k_m l_3} - e^{-k_m l_4}) (P_{2m} e^{K_{1m} z} + P_{3m} e^{-K_{1m} z})$$

$$Z(\omega) = Z_0 + \sum_{i=1}^N \sum_{m=1}^{\infty} \left\{ \frac{j2\pi\omega\mu_0 I(r_{1i}, r_{2i}) \sum_{i=1}^N I(kr_{1i}, kr_{2i})}{(l_2 - l_1)^2 (r_{2i} - r_{1i})^2 k_m^7 R^2 J_0^2(k_m R)} \cdot \right.$$

$$[2(l_2 - l_1) + 2(e^{-k(l_2 - l_1)} - 1) + (e^{-kl_1} - e^{-kl_2})(e^{kl_4} - e^{kl_3})$$

$$+ P_{1m}(e^{-kl_1} - e^{-kl_2} + e^{-kl_3} - e^{-kl_4})(e^{-kl_1} - e^{-kl_2})]$$

$$+ \frac{j2\pi\omega\mu_0 I(r_{1i}, r_{2i}) \sum_{i=1}^N I(kr_{1i}, kr_{2i})}{(l_4 - l_3)^2 (r_{2i} - r_{1i})^2 k_m^7 R^2 J_0^2(k_m R)} [2(l_4 - l_3)] \quad (2.91)$$

$$+ \frac{j2\pi\omega\mu_0 I(r_{1i}, r_{2i}) \sum_{i=1}^N I(kr_{1i}, kr_{2i})}{(l_4 - l_3)^2 (r_{2i} - r_{1i})^2 k_m^7 R^2 J_0^2(k_m R)} [2(l_4 - l_3)$$

$$+ 2(e^{-k(l_4 - l_3)} - 1) + (e^{-kl_1} - e^{-kl_2})(e^{kl_4} - e^{kl_3})$$

$$+ P_{1m}(e^{-kl_3} - e^{-kl_4} + e^{-kl_1} - e^{-kl_2})(e^{-kl_3} - e^{-kl_4})]$$

2.4.3 The Time-Domain Solutions

Pulsed excitations and responses can be expressed as the superposition of a series of sinusoidal signals with different frequencies. When the frequency-domain expressions of magnetic flux density and pulsed eddy current are known, their time-domain expressions can be obtained by the inverse Fourier transformation.

For (2.88), (2.89), and (2.90), the corresponding time-domain expressions can be obtained.

$$B_r(t, k, z) = \frac{1}{2\pi} \int_{-\infty}^{\infty} B_r(\omega, k, z) e^{j\omega t} d\omega \quad (2.92)$$

$$B_z(t, r, z) = \frac{1}{2\pi} \int_{-\infty}^{\infty} B_z(\omega, r, z) e^{j\omega t} d\omega \quad (2.93)$$

$$J_e(t, r, z) = \frac{1}{2\pi} \int_{-\infty}^{\infty} J_e(\omega, r, z) e^{j\omega t} d\omega \quad (2.94)$$

(2.92), (2.93), and (2.94) are difficult to analytically implement for the infinite integration of the integrands $B_r(\omega, r, z)$, $B_z(\omega, r, z)$, and $J_e(\omega, r, z)$ with such complex expressions. The FFT and IFFT methods are good choices for their calculation. The procedure is that the time-domain current excitation signal is transformed to the frequency domain by FFT, and then, the magnetic flux densities and eddy currents at chosen frequencies are calculated according to (2.88), (2.89), and (2.90) and summed. Lastly, the time-domain responses of the magnetic flux density and pulsed eddy current are obtained by IFFT of the summed frequency-domain signals.

When the pulsed eddy current in the skin depth of the specimen is known, the *Lorentz force* can be calculated using (2.95).

$$f_L(t, r, z) = B_0 \times J_e(t, r, z) \quad (2.95)$$

In the above equation, $f_L(t, r, z)$ represents the *Lorentz force* and B_0 represents the bias static magnetic flux density.

2.4.4 Results Comparison and Discussion

In order to validate the proposed analytical model and calculation method, an example is demonstrated. Moreover, the results are compared to those of the TSFEM method and experiment.

A double-layer PCB spiral coil, shown in Fig. 2.24, is used for the calculation. The specimen is an aluminum plate. The liftoff distance between the coil and specimen is 0.5 mm. The infinite half-space below the aluminum plate is air. The dimensions and properties of the coil and specimen employed in the simulation and experiment are shown in Tables 2.4 and 2.5.

Generally, the EMATs are supplied by narrow pulses or modulated tone-burst signals, which are generated by the function generator and amplified by the power amplifier.

The modulated tone-burst current signal can be expressed using (2.96).

Fig. 2.24 Double-layer PCB spiral coil above the specimen

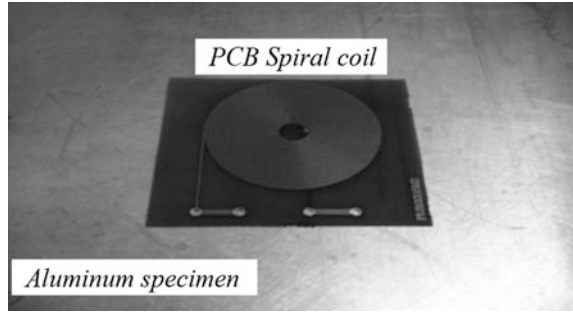


Table 2.4 The width of the double-layer spiral coil and the material parameters

Parameter name	Value
Substrate thickness	0.500 mm
Copper wire width	0.254 mm
Copper wire thickness	0.050 mm
r_{11}	2.921 mm
r_{21}	3.175 mm
The conductor's ring space	0.254 mm
Number of turns	29
Copper wire's magnetic permeability	$4\pi \times 10^{-7}$ H/m
Copper wire's electric conductivity	2.66×10^7 S/m

Table 2.5 The specimen's dimension and the material's parameters

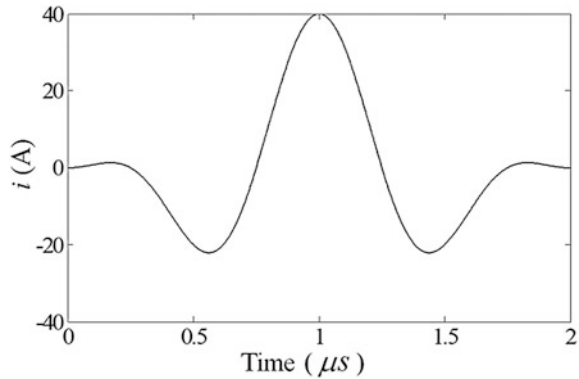
Parameter name	Value
Specimen's thickness	5.00 mm
Magnetic permeability	$4\pi \times 10^{-7}$ H/m
Electric conductivity	3.571×10^{-7} S/m

$$i(t) = \begin{cases} I_0 \left(1 - \cos \frac{\omega t}{n}\right) \cos \omega t & 0 \leq t \leq \frac{2n\pi}{\omega} \\ 0 & t \geq \frac{2n\pi}{\omega} \end{cases} \quad (2.96)$$

In the above equation, $\omega = 2\pi f$. Here, $I_0 = 20A$, $n = 2$, and $f = 1$ MHz were selected; the waveform of the pulsed current signal is shown as follows (Fig. 2.25):

In the calculation process, the truncation radius is $R = 696$ mm and the summation number is 50. The sampling frequency and data number used in the FFT-IFFT method are chosen as 32 MHz and 64, respectively. Then, an impedance analyzer is used to measure the resistance and inductance of the coil above the specimen, so that the input impedance of the EMAT can be obtained. The time-domain response of the magnetic flux density and pulsed eddy current calculated by the TSFEM method is implemented through the FEM analysis software. To improve the accuracy, a denser mesh is used in the coil cross section and surface of the specimen. The number of the overall triangular elements is 13,193.

Fig. 2.25 The waveform of the tone-burst signal supplied to the spiral coil. The center frequency of the signal is 1 MHz and the number of periods is 2



To design the matching circuits for the EMATs, the impedance of the coil at the center frequency needs to be determined. Here, for validating the input impedance expressions as (2.81) and (2.91), the input impedance at frequencies 0.5, 1, and 1.5 MHz are calculated and then measured by the impedance analyzer. The results are shown in Table 2.6.

As shown in Table 2.6, the calculated results and measured results are in agreement, which validates the validity and accuracy of the input impedance expressions and the TREE method.

The transient time-domain signals of B_r , B_z , and J_e from both the proposed method and the TSFEM method are presented in Figs. 2.20, 2.21, and 2.22.

As shown in Figs. 2.26, 2.27, and 2.28, the results from the proposed method are consistent with those from the TSFEM method. The small discrepancies are that as follows: (1) B_r and B_z from the proposed method are a little larger than those from the TSFEM method, while J_e has the opposite relationship, and (2) the peak value times and the waveforms in the initial stage have certain differences. An evaluation of the errors of peak values and peak value times is shown in Table 2.7.

Assuming that the bias magnetic field is uniform and equals 1 T, we calculate the *Lorentz force* on the surface of the specimen according to Eq. (2.95). The *Lorentz force* inside the specimens under different liftoff values is shown in the following figure.

As shown in Fig. 2.29, it is found that *Lorentz force* will decrease with an increase in the liftoff distance. If the *Lorentz force* is given, the particle's

Table 2.6 Input impedance by calculation and measurement at different frequency

Frequency (MHz)	Calculation value (Ω)	Measuring value (Ω)
0.5	$12.51 + j30.64$	$13.03 + j31.34$
1	$13.19 + j60.34$	$13.89 + j63.25$
1.5	$13.71 + j89.87$	$14.75 + j93.80$

Fig. 2.26 Magnetic flux densities in the r direction at position (3.048 mm, -0.001 mm) on the surface of the specimen

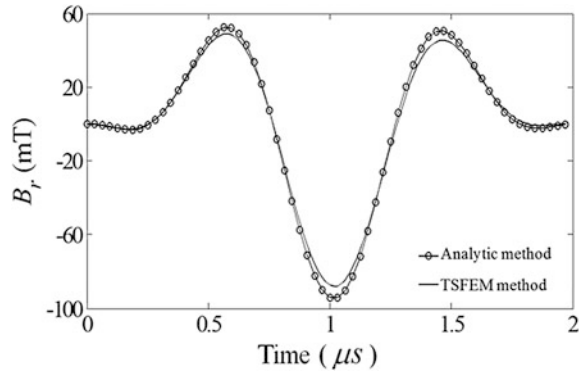


Fig. 2.27 Magnetic flux densities in the z direction at position (3.048 mm, -0.001 mm) on the surface of the specimen

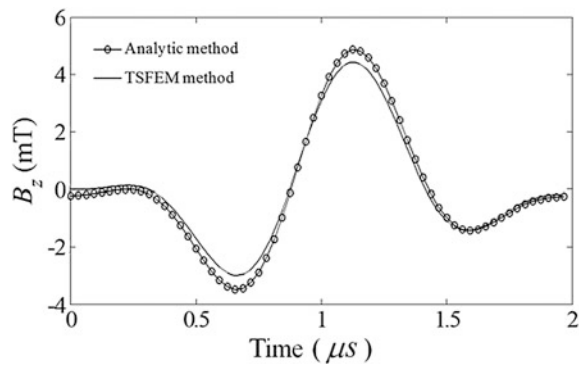


Fig. 2.28 Magnetic flux densities at position (3.048 mm, -0.001 mm) on the surface of the specimen

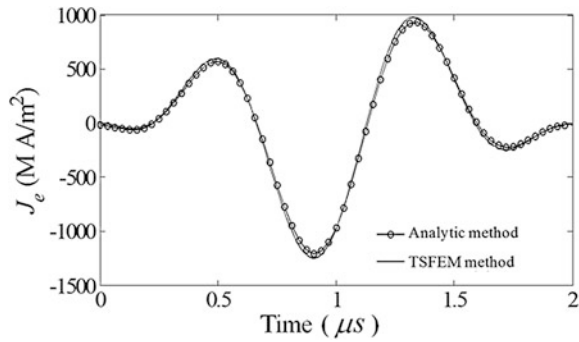
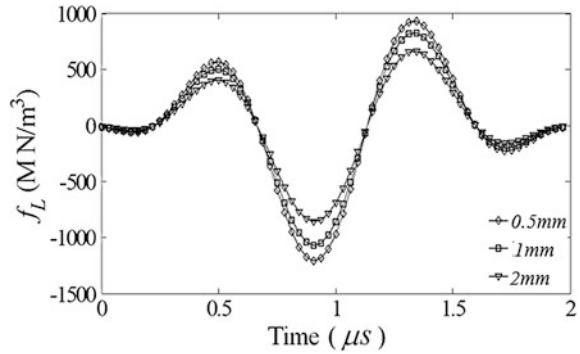


Table 2.7 Errors of peak value and peak value time comparing two methods

Error	B_r	B_z	J_e
Waveform peak	7.4	9.7	3.1
Waveform peak's time	0.78	1.3	0.41

Fig. 2.29 Lorentz force at position (3.048 mm, -0.01 mm) on the surface of the specimen calculated by the proposed method when the liftoff distances are 0.5, 1, and 2 mm



displacement can be calculated according to the theory of elasticity for *Lorentz force mechanism* EMATs.

Although the analytical expressions of magnetic flux density, pulsed eddy current, and input impedance are complicated, they are valid and accurate when calculated by TREE and FFT-IFFT method, which is entirely much simpler than the TSFEM method. Moreover, the distinct mathematical expressions and faster calculation speed are also advantages over the TSFEM method.

The following causes could result in errors between calculation results and measurement results. The coil's skin effect and proximity effect were overlooked in the analytic model, which might cause certain errors in the circumstance of high frequency; in addition, some errors could be caused by the TREE method itself.

2.5 Analytical Modeling and Calculation of the Meander Coil EMAT [4]

In the field of nondestructive testing with EMAT under different static bias magnetic fields, the meander coil EMAT has an important position and is widely used for generating and detecting various types of ultrasonic waves, such as the *Lamb wave*, *Rayleigh wave*, and *shear horizontal* (SH) wave. The analytical model and analysis of EMAT with a meander coil structure will be illustrated in this section.

2.5.1 Meander Coil EMAT Configuration and Calculation Model

Nowadays, with the development of printed circuit boards (PCB) or flexible print circuit (FPC) techniques, the meander coil can be made more complex, accurate, and portable to improve the performance of EMAT and facilitate its actual application. The typical configurations of a meander coil are shown in Fig. 2.30.

The purpose of the multisplit configuration of a meander coil is to increase the turn number of each fold. For the same reason, sometimes, the coil is designed into a multilayer configuration, using the configuration of equidistance or non-equidistance to control the excited ultrasonic wave modes through controlling the coil's spacing.

When used for ultrasonic wave generation and detection, the meander coils are placed parallel above the surface of the specimen. If we neglect the ends connection of the meander coil, the section diagram of the EMAT is as shown in Fig. 2.31. We assume that the meander coil is an M -layer, N -conductor coil, and the number of bends is $2Q$. This model is the general model of the meander coil. The coil with an equidistance structure is a special case.

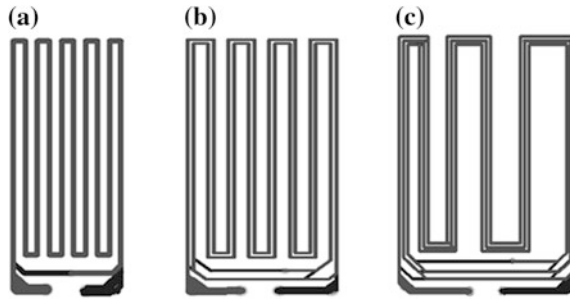


Fig. 2.30 Configuration of meander coils: **a** Isometric single-split coil; **b** Isometric multisplit coil; **c** Non-equidistance multisplit coil

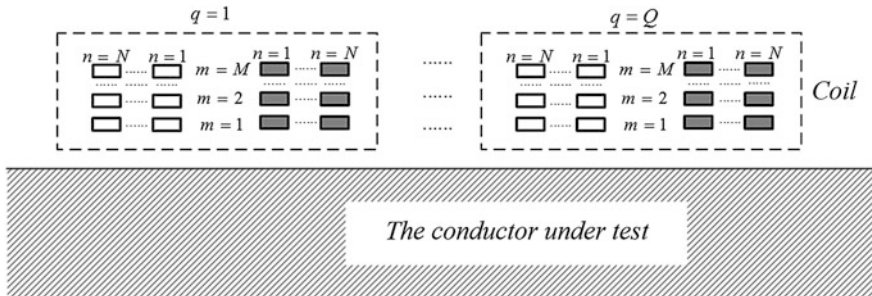


Fig. 2.31 Model of a meander coil EMAT

As shown in Fig. 2.31, according to the characteristics of the meander coil, the current directions in the two adjacent bends of the coil are opposite to each other. Therefore, the adjacent bends can be viewed as a closed coil. Thus, the M -layer, N -conductor coil can be viewed as the group of $M \times N \times Q$ single rectangular coils.

2.5.2 The Frequency-Domain Calculation of the Coil's Impedance and Magnetic Field

2.5.2.1 The Scalar Potential of the Rectangle δ Coil

The schematic diagram of a δ coil with current I above an infinite half-space is shown in Fig. 2.32. The solution domain is divided into three subdomains: the domain above the δ coil R_a , the domain between the δ coil and the conductor R_b , and the conductor domain R_c . In Fig. 2.32, x_0 and y_0 indicate the half width and length of the δ coil.

Because the frequencies in the EMAT nondestructive testing are generally lower than 10 MHz, the displacement current and velocity effect can be neglected; thus, the time-harmonic electromagnetic field governing equation is expressed in (2.97).

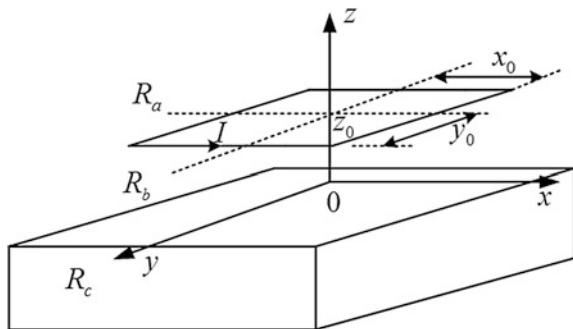
$$\nabla^2 A + \gamma^2 A = -\mu J_s \quad (2.97)$$

In the above equation, A is the magnetic vector potential; J_s is the source current density; $\gamma^2 = -j\omega\mu\sigma$; ω is the angular frequency; μ is the medium permeability; σ is the medium conductivity, and ∇^2 is the Laplace operator.

In terms of Coulomb's criteria $\nabla \cdot A = 0$, there is a second vector potential W , which satisfies $A = \nabla \times W$, and W can be decomposed as two scalar potentials. W can be expressed using (2.98).

$$W = uW_1 + u \times \nabla W_2 \quad (2.98)$$

Fig. 2.32 Rectangle δ coil above the conductor



In the above equation, W_1 and W_2 are scalar potentials and u is the vector that meets the requirement.

We choose $u = \hat{z}$, A can be expressed by the second vector potential W .

$$A = \nabla \times (W_1 \hat{z} + \hat{z} \times \nabla W_2) \quad (2.99)$$

Substituting (2.99) into (2.97), we can obtain (2.100).

$$\nabla \times [\hat{z} \nabla^2 W_1 + \hat{z} \times \nabla (\nabla^2 W_2) + \gamma^2 (W_1 \hat{z} + \hat{z} \times \nabla W_2)] = -\mu J_s \quad (2.100)$$

In the air domains R_a and R_b , the source current density and conductivity are 0; thus, we have (2.101), (2.102), and (2.103).

$$\nabla^2 W_{1(a,b)} = 0 \quad (2.101)$$

$$\nabla^2 W_{2(a,b)} = 0 \quad (2.102)$$

$$A_{(a,b)} = \nabla \times (W_{1(a,b)} \hat{z}) - (\hat{z} \cdot \nabla) \nabla W_{2(a,b)} \quad (2.103)$$

In the above equations, the subscript (a,b) represents the variables in domains a and b ; thus, we have (2.104).

$$B_{(a,b)} = \nabla \left(\frac{\partial W_{1(a,b)}}{\partial z} \right) \quad (2.104)$$

Therefore, we just need to calculate the scalar potential $W_{1(a,b)}$, which is the superposition of the coil's scalar potential $W_{1(a,b)s}$ and the eddy current's scalar potential $W_{1(a,b)e}$, as expressed in (2.105).

$$W_{1(a,b)} = W_{1(a,b)s} + W_{1(a,b)e} \quad (2.105)$$

Thus, we have (2.106).

$$\nabla^2 (W_{1(a,b)s} + W_{1(a,b)e}) = 0 \quad (2.106)$$

In domain R_c , according to the interface conditions, in interface $z = 0$, the $W_{2(c)}$ should satisfy (2.107).

$$\begin{cases} \frac{\partial W_{2(e)}}{\partial z} = 0 \\ W_{2(e)} = 0 \end{cases} \quad (2.107)$$

In the above equation, the subscript (c) represents the variables in domain c . Since there is no source in domain R_c , $W_{2(e)} = 0$; thus, we have (2.108).

$$A_{(c)} = \nabla \times (W_{1(c)} \hat{z}) \quad (2.108)$$

According to (2.100), we obtain (2.109).

$$\nabla^2 W_{1(c)} + \Upsilon^2 W_{1(c)} = 0 \quad (2.109)$$

Therefore, when we calculate the magnetic field of the δ coil, we just need to calculate W_1 in terms of (2.106) and (2.109).

The general solutions of (2.106) and (2.109) can be expressed as the forms of the double *Fourier* integral, which are shown in (2.110), (2.111) and (2.112).

$$W_{1(b)s} = \int_{-\infty}^{+\infty} \int_{-\infty}^{+\infty} C(\alpha, \beta) e^{kz} e^{j\alpha x} e^{j\beta y} d\alpha d\beta \quad (2.110)$$

$$W_{1(b)e} = \int_{-\infty}^{+\infty} \int_{-\infty}^{+\infty} C(\alpha, \beta) \frac{k\mu_r - \lambda}{k\mu_r + \lambda} e^{-kz} e^{j\alpha x} e^{j\beta y} d\alpha d\beta \quad (2.111)$$

$$W_{1(e)} = \int_{-\infty}^{+\infty} \int_{-\infty}^{+\infty} C(\alpha, \beta) \frac{2k\mu_r}{k\mu_r + \lambda} e^{\lambda z} e^{j\alpha x} e^{j\beta y} d\alpha d\beta \quad (2.112)$$

In the above equations, α and β are integral variables; $C(\alpha, \beta)$ is the undetermined coefficient; $k = \sqrt{\alpha^2 + \beta^2}$; and $\lambda = \sqrt{k^2 + \gamma^2}$. From the above three equations, when the coefficients are determined, the scalar potential W_1 of the whole domain can be calculated.

According to the *Biot–Savart* theorem, we get (2.113).

$$B_{(a,b)s} = \nabla \times \frac{\mu_0 I}{4\pi} \oint_l \frac{d\mathbf{l}}{r} \quad (2.113)$$

In the above equation, $r = \sqrt{(x - x_0)^2 + (y - y_0)^2 + (z - z_0)^2}$ is the distance between *point* (x, y, z) and *point* (x_0, y_0, z_0) ; μ_0 is the vacuum permeability, and l is the integral path.

The Stokes theorem is used for the above equation, so that we get (2.114).

$$B_{(a,b)s} = \nabla \left[-\frac{\mu_0 I}{4\pi} \iint_{\Omega} d\mathbf{s} \cdot \nabla \left(\frac{1}{r} \right) \right] \quad (2.114)$$

In the above equation, Ω represents the arbitrary curved surfaces encircled by l . Comparing (2.103) and (2.113), we get (2.115).

$$W_{1(a,b,s)} = -\frac{\mu_0 I}{4\pi} \iint_S ds \cdot \nabla \left(\int \frac{dz}{r} \right) \quad (2.115)$$

In the above equation, we have the following relationship, as shown in (2.116).

$$\frac{1}{r} = \frac{1}{2\pi} \int_{-\infty}^{+\infty} \int_{-\infty}^{+\infty} \frac{e^{\mp k(z-z_0)}}{k} e^{j[\alpha(x-x_0) + \beta(y-y_0)]} d\alpha d\beta \quad (2.116)$$

Substituting (2.116) into (2.115), we obtain (2.117) and (2.118).

$$W_{1(a)s} = \frac{\mu I}{2\pi^2} \int_{-\infty}^{+\infty} \int_{-\infty}^{+\infty} \frac{e^{-k(z-z_0)}}{k} \frac{\sin(\alpha y_0)}{\alpha} \times \frac{\sin(\beta y_0)}{\beta} e^{j\alpha x} e^{j\beta y} d\alpha d\beta \quad (2.117)$$

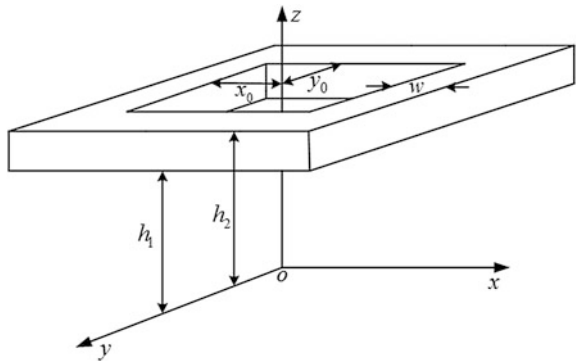
$$W_{1(b)s} = \frac{\mu I}{2\pi^2} \int_{-\infty}^{+\infty} \int_{-\infty}^{+\infty} \frac{e^{k(z-z_0)}}{k} \frac{\sin(\alpha y_0)}{\alpha} \times \frac{\sin(\beta y_0)}{\beta} e^{j\alpha x} e^{j\beta y} d\alpha d\beta \quad (2.118)$$

2.5.2.2 Scalar Potential of Rectangular Single-Turn Coil

Firstly, considering the single-turn coil, the configuration is as shown in Fig. 2.33. In Fig. 2.33, x_0 and y_0 represent the distance from the inner edge to the z axis in length and width directions, respectively; w represents the width of the coil conductor, and h_1 and h_2 represent the distance from the xoy plane to the upper and lower edges, respectively.

The scalar potential of the single-turn coil can be viewed as the superposition of those δ coils. If we assume that the current density in the section of the conductor is continuous, we can get (2.119).

Fig. 2.33 Rectangular single-turn coil



$$W_{1(a,b)s}^S = \int_0^w \int_{h_1}^{h_2} W_{1(a,b)s} dz_0 dw \quad (2.119)$$

In the above equation, the superscript S represents the single-turn coil.

Substituting (2.117) and (2.118) into (2.119), and calculating the integral, we can get (2.120) and (2.121).

$$W_{1(a)s}^S = \frac{\mu_0 I}{2\pi^2(h_2 - h_1)w} \int_{-\infty}^{+\infty} \int_{-\infty}^{+\infty} \frac{e^{-kz}}{k^2} (e^{kh_2} - e^{kh_1}) \frac{P}{\alpha\beta} e^{j\alpha x} e^{j\beta y} d\alpha d\beta \quad (2.120)$$

$$W_{1(b)s}^S = \frac{\mu_0 I}{2\pi^2(h_2 - h_1)w} \int_{-\infty}^{+\infty} \int_{-\infty}^{+\infty} \frac{e^{kz}}{-k^2} (e^{-kh_2} - e^{-kh_1}) \frac{P}{\alpha\beta} e^{j\alpha x} e^{j\beta y} d\alpha d\beta \quad (2.121)$$

In the above two equations, there is some relationship, as follows.

$$P = \begin{cases} \frac{\sin[(\alpha - \beta)w + \alpha x_0 - \beta y_0] - \sin(\alpha x_0 - \beta y_0)}{2(\alpha - \beta)} \\ - \frac{\sin[(\alpha + \beta)w + \alpha x_0 + \beta y_0] - \sin(\alpha x_0 + \beta y_0)}{2(\alpha + \beta)} & \alpha \neq \beta \\ \frac{w}{2} \cos[\alpha(x_0 - y_0)] \\ - \frac{\sin[\alpha(2w + x_0 + y_0)] - \sin[\alpha(x_0 + y_0)]}{4\alpha} & \alpha = \beta \end{cases}$$

(2.120) and (2.121) give the scalar potentials above and under the coil. For the domain in the section of the coil, the scalar potential in an arbitrary *point* (x, y, z) can be obtained by superpositioning the scalar potential above and under the coil, and then substituting $h_2 = z$ and $h_1 = z$ into (2.120) and (2.121) separately, and summing them, to get (2.122).

$$W_{1\text{coilsection}} = \frac{\mu_0 I}{2\pi^2(h_2 - h_1)w} \int_{-\infty}^{+\infty} \int_{-\infty}^{+\infty} \frac{1}{k^2} [2 - e^{-k(z-h_1)}] \\ - e^{k(z-h_2)} \frac{P}{\alpha\beta} e^{j\alpha x} e^{j\beta y} d\alpha d\beta \quad (2.122)$$

When the center coordinates of the single-turn coil are (x', y', z_0) , we can supplement the term $e^{-j\alpha x'} e^{-j\beta y'}$ in (2.120), (2.121), and (2.122) according to coordinate transformation.

2.5.2.3 Scalar Potential of Meander Coil

When the scalar potential of the single-turn coil is obtained, the scalar potential of the meander coil can be obtained by coordinate transformation and superposition.

For the configuration of the meander coil shown in Fig. 2.25, we assume the center coordinate of group ($q = 1$) is $(0, 0, z_m)$; thus, the center coordinates of group ($q = 2 \sim Q$) are $(x_q', 0, z_m)$. In each layer, there are $N \times Q$ single-turn coils; thus, the scalar potential in the m layer can be expressed by (2.123), (2.124), and (2.125).

$$W_{1(a)s}^m = \frac{\mu_0 I}{2\pi^2(h_2 - h_1)w} \int_{-\infty}^{+\infty} \int_{-\infty}^{+\infty} \frac{e^{-kz}}{k^2} (e^{kh_m} - e^{kh_{1m}}) \frac{\sum_{n=1}^N P_n}{\alpha\beta} \sum_{q=1}^Q e^{-j\alpha x'} e^{j\alpha x} e^{j\beta y} d\alpha d\beta \quad (2.123)$$

$$W_{1(b)s}^m = \frac{\mu_0 I}{2\pi^2(h_2 - h_1)w} \int_{-\infty}^{+\infty} \int_{-\infty}^{+\infty} \frac{e^{kz}}{k^2} (e^{-kh_{2m}} - e^{-kh_{1m}}) \frac{\sum_{n=1}^N P_n}{\alpha\beta} \sum_{q=1}^Q e^{-j\alpha x'_q} e^{j\alpha x} e^{j\beta y} d\alpha d\beta \quad (2.124)$$

$$W_{1coilsection}^m = \frac{\mu_0 I}{2\pi^2(h_2 - h_1)w} \int_{-\infty}^{+\infty} \int_{-\infty}^{+\infty} \frac{1}{k^2} \left(2 - e^{-k(z-h_{2m})} - e^{-k(z-h_{1m})} \right) \frac{\sum_{n=1}^N P_n}{\alpha\beta} \sum_{q=1}^Q e^{-j\alpha x'_q} e^{j\alpha x} e^{j\beta y} d\alpha d\beta \quad (2.125)$$

In the above equations, there is some relationship, as follows, in which the superscript m represents the layer.

$$P_n = \begin{cases} \frac{\sin[(\alpha - \beta)w + \alpha x_{0n} - \beta y_{0n}] - \sin(\alpha x_{0n} - \beta y_{0n})}{2(\alpha - \beta)} & \alpha \neq \beta \\ -\frac{\sin[(\alpha + \beta)w + \alpha x_{0n} + \beta y_{0n}] - \sin(\alpha x_{0n} + \beta y_{0n})}{2(\alpha + \beta)} & \alpha \neq \beta \\ \frac{w}{2} \cos[\alpha(x_{0n} - y_{0n})] & \alpha = \beta \\ -\frac{\sin[\alpha(2w + x_{0n} + y_{0n})] - \sin[\alpha(x_{0n} + y_{0n})]}{4\alpha} & \alpha = \beta \end{cases}$$

The scalar potential in domain R_b can be obtained by the superposition of the scalar potential of each area, as shown in (2.126).

$$\begin{aligned}
 W_{1(b)s} = & \frac{\mu_0 I}{2\pi^2(h_2 - h_1)w} \int_{-\infty}^{+\infty} \int_{-\infty}^{+\infty} \frac{e^{kz}}{-k^2} \sum_{m=1}^M (e^{-kh_{2m}} - e^{-kh_{1m}}) \\
 & \times \frac{1}{\alpha\beta} \sum_{n=1}^N P_n \sum_{q=1}^Q e^{-j\alpha x'_q} e^{j\alpha x} e^{j\beta y} d\alpha d\beta
 \end{aligned} \quad (2.126)$$

Comparing the above equation and (2.110), the coefficient $C(\alpha, \beta)$ can be obtained, as shown in (2.127).

$$C(\alpha, \beta) = -\frac{\mu_0 I}{2\pi^2(h_2 - h_1)wk^2\alpha\beta} \sum_{m=1}^M (e^{-kh_{2m}} - e^{-kh_{1m}}) \sum_{n=1}^N P_n \sum_{q=1}^Q e^{-j\alpha x'_q} \quad (2.127)$$

Then, $W_{1(b)s}$ and $W_{1(c)}$ can be obtained by substituting Eq. (2.127) into (2.111) and (2.112), separately.

For the meander coil, it is worth paying attention to the magnetic field of each layer of conductor coil. For each layer of coil, the scalar potential of the conductor's region is equal to the sum of the scalar potential generated by the layer itself and coils of other layers; thus, the equation for the area of the coil of the m th layer is listed in (2.128), in which the superscript m represents the layer.

$$\begin{aligned}
 W_{lcoilsection}^{m'} = & \frac{\mu_0 I}{2\pi^2(h_2 - h_1)w} \int_{-\infty}^{+\infty} \int_{-\infty}^{+\infty} \left\{ \frac{1}{k^2} \left[2 - e^{-k(z-h_{1m'})} - e^{k(z-h_{2m'})} \right] \right. \\
 & + \sum_{m=1}^{m'-1} \frac{e^{-kz}}{k^2} (e^{kh_{2m}} - e^{kh_{1m}}) - \sum_{m=m'+1}^M \frac{e^{kz}}{k^2} (e^{-kh_{2m}} - e^{-kh_{1m}}) \left. \right\} \\
 & \times \frac{1}{\alpha\beta} \sum_{n=1}^N P_n \sum_{q=1}^Q e^{-j\alpha x'_q} e^{j\alpha x} e^{j\beta y} d\alpha d\beta
 \end{aligned} \quad (2.128)$$

2.5.2.4 Eddy Current, Magnetic Flux Density, and Coil's Impedance

The eddy current is induced into the tested conductor, which is necessary for the electromagnetic ultrasonic testing. According to electromagnetic field theory, the eddy current generated by the meander coil on the surface of the conductor can be calculated by (2.129), in which J_e represents the eddy current in the conductor.

$$J_e = -j\omega\sigma A_{(c)} \quad (2.129)$$

Substituting (2.102) into (2.129), we can obtain (2.130), in which \hat{x} and \hat{y} are direction vectors.

$$\begin{aligned}
J_e = & \frac{j\omega\sigma\mu_0 I}{\pi^2(h_2 - h_1)w} \int_{-\infty}^{+\infty} \int_{-\infty}^{+\infty} \frac{e^{\lambda z}}{k} \times \frac{\mu_r}{k\mu_r + \lambda} \\
& \times (j\beta\hat{x} - j\alpha\hat{y}) \sum_{m=1}^M (e^{-kh_{2m}} - e^{-kh_{1m}}) \\
& \times \frac{1}{\alpha\beta} \sum_{n=1}^N P_n \sum_{q=1}^Q e^{-j\alpha x'_q} e^{j\alpha x} e^{j\beta y} d\alpha d\beta
\end{aligned} \tag{2.130}$$

According to (2.104), (2.112), (2.125), and (2.126), the magnetic flux density can be obtained within domain R_b and R_c , as shown in (2.131) and (2.132).

$$\begin{aligned}
B_{(b)} = & \frac{\mu_0 I}{2\pi^2(h_2 - h_1)w} \int_{-\infty}^{+\infty} \int_{-\infty}^{+\infty} \left[\frac{1}{-k} \left(e^{kz} - \frac{k\mu_r - \lambda}{k\mu_r + \lambda} e^{-kz} \right) \right. \\
& \times (j\alpha\hat{x} + j\beta\hat{y}) - \left. \left(e^{kz} + \frac{k\mu_r - \lambda}{k\mu_r + \lambda} e^{-kz} \right) \hat{z} \right] \\
& \sum_{m=1}^M (e^{-kh_{2m}} - e^{-kh_{1m}}) \times \frac{1}{\alpha\beta} \sum_{n=1}^N P_n \sum_{q=1}^Q e^{-j\alpha x'_q} e^{j\alpha x} e^{j\beta y} d\alpha d\beta
\end{aligned} \tag{2.131}$$

$$\begin{aligned}
B_{(c)} = & \frac{\mu_0 I}{2\pi^2(h_2 - h_1)w} \int_{-\infty}^{+\infty} \int_{-\infty}^{+\infty} \left[\frac{e^{\lambda z}}{-k} \times \frac{2k\mu_r\lambda}{k\mu_r + \lambda} \right. \\
& \times (j\alpha\hat{x} + j\beta\hat{y} + \lambda\hat{z}) \left. \sum_{m=1}^M (e^{-kh_{2m}} - e^{-kh_{1m}}) \right] \\
& \times \frac{1}{\alpha\beta} \sum_{n=1}^N P_n \sum_{q=1}^Q e^{-j\alpha x'_q} e^{j\alpha x} e^{j\beta y} d\alpha d\beta
\end{aligned} \tag{2.132}$$

The coil's impedance can be expressed as the sum of the coil's DC impedance, the coil's impedance in free space, and the impedance generated by the eddy current induced by the conductor, as shown in (2.133).

$$Z = Z_d + Z_0 + \Delta Z \tag{2.133}$$

In the above equation, Z_d is the DC impedance; Z_0 is the impedance in free space, and ΔZ is the impedance generated by the eddy current.

Impedance Z_0 can be calculated by (2.134).

$$Z_0 = \frac{V}{I} \tag{2.134}$$

Therefore, if we want to calculate Z_0 , it is necessary to calculate the electromotive force first. According to the idea of scalar potential calculation, the electromotive force of the single-turn coil should be calculated first, as shown in (2.135).

$$V^S = \frac{j\omega}{(h_2 - h_1)w} \int_{\text{coilcrosssection}} \left(\int_S B \cdot ds \right) d\text{Area} \quad (2.135)$$

The electromotive force of the meander coil is the superposition of the electromotive force of all equivalent rectangular coils; thus, we have (2.136).

$$\begin{aligned} V = & \frac{2j\omega\mu_0 I}{\pi^2(h_2 - h_1)^2 w^2} \sum_{m'=1}^M \int_{-\infty}^{+\infty} \int_{-\infty}^{+\infty} \left\{ 2(h_{2m'} - h_{1m'}) \right. \\ & + \frac{2}{k} \left[e^{-k(h_{2m'} - h_{1m'})} - 1 \right] + \sum_{m=1}^{m'-1} \frac{1}{k} (e^{kh_{2m}} - e^{kh_{1m}}) (e^{-kh_{1m'}} - e^{-kh_{2m'}}) \\ & + \left. \sum_{m=m'+1}^M \frac{1}{k} (e^{-kh_{2m}} - e^{-kh_{1m}}) (e^{kh_{1m'}} - e^{kh_{2m'}}) \right\} \\ & \times \frac{1}{(\alpha\beta)^2} \left(\sum_{n=1}^N P_n \right)^2 \left(\sum_{q=1}^Q e^{-j\alpha x'_q} + \sum_{q=1}^Q e^{j\alpha x'_q} \right) d\alpha d\beta \end{aligned} \quad (2.136)$$

Thus, according to (2.134), we can get (2.137).

$$\begin{aligned} Z_0 = & \frac{2j\omega\mu_0}{\pi^2(h_2 - h_1)^2 w^2} \sum_{m'=1}^M \int_{-\infty}^{+\infty} \int_{-\infty}^{+\infty} \left\{ 2(h_{2m'} - h_{1m'}) \right. \\ & + \frac{2}{k} \left[e^{-k(h_{2m'} - h_{1m'})} - 1 \right] + \sum_{m=1}^{m'-1} \frac{1}{k} (e^{kh_{2m}} - e^{kh_{1m}}) (e^{-kh_{1m'}} - e^{-kh_{2m'}}) \\ & + \left. \sum_{m=m'+1}^M \frac{1}{k} (e^{-kh_{2m}} - e^{-kh_{1m}}) (e^{kh_{1m'}} - e^{kh_{2m'}}) \right\} \\ & \times \frac{1}{(\alpha\beta)^2} \left(\sum_{n=1}^N P_n \right)^2 \left(\sum_{q=1}^Q e^{-j\alpha x'_q} + \sum_{q=1}^Q e^{j\alpha x'_q} \right) d\alpha d\beta \end{aligned} \quad (2.137)$$

(2.138) can be used to calculate the impedance ΔZ .

$$\Delta Z = \Delta R + j\Delta X = \frac{j8\pi^2\omega}{\mu_0 i^2} \int_{-\infty}^{+\infty} \int_{-\infty}^{+\infty} k^3 C(\alpha, \beta) \times C(-\alpha, -\beta) \frac{k\mu_r - \lambda}{k\mu_r + \lambda} d\alpha d\beta \quad (2.138)$$

Substituting $C(\alpha, \beta)$ into the above equation, we obtain (2.139).

$$\Delta Z = \frac{j2\omega\mu_0}{\pi^2(h_2 - h_1)^2 w^2} \int_{-\infty}^{+\infty} \int_{-\infty}^{+\infty} \frac{1}{k(\alpha\beta)^2} \left[\sum_{m=1}^M (e^{-kh_{2m}} - e^{-kh_{1m}}) \right]^2 \left(\sum_{n=1}^N P_n \right)^2 \left(\sum_{q=1}^Q e^{-j\alpha x'_q} \times \sum_{q=1}^Q e^{j\alpha x'_q} \right) \times \frac{k\mu_r - \lambda}{k\mu_r + \lambda} d\alpha d\beta \quad (2.139)$$

The meander coil's DC impedance Z_d is DC resistance, which can be calculated by the coil's dimension and electrical conductivity, as shown in (2.140).

$$Z_d = \frac{L}{\sigma_c(h_2 - h_1)w} \quad (2.140)$$

In the above equation, L is the total length of the meander coil conductor and σ_c is the electrical conductivity of the coil conductor.

2.5.3 The Calculation of the Time-Domain Pulsed Magnetic Field

In the electromagnetic ultrasonic testing, the applied excitation is a pulse signal. The pulsed magnetic field generated by the coil and the eddy current in the specimen should be calculated, that is, the pulsed response should be calculated.

The pulsed excitation and the corresponding pulsed response can be expressed as the superposition of a series of sinusoidal signals of different frequencies. For the conditions of the expressions of magnetic induction intensity and eddy current, the time-domain response can be obtained by the inverse Fourier transformation (IFT), as shown in (2.141), (2.142), and (2.143).

$$J_e(t) = \frac{1}{2\pi} \int_{-\infty}^{\infty} J_e e^{j\omega t} d\omega \quad (2.141)$$

$$B_{(b)}(t) = \frac{1}{2\pi} \int_{-\infty}^{\infty} B_{(b)} e^{j\omega t} d\omega \quad (2.142)$$

$$B_{(c)}(t) = \frac{1}{2\pi} \int_{-\infty}^{\infty} B_{(c)} e^{j\omega t} d\omega \quad (2.143)$$

In the above equations, $J_e(t)$, $B_{(b)}(t)$, and $B_{(c)}(t)$ represent the time-domain signals of the eddy current and magnetic flux density, respectively.

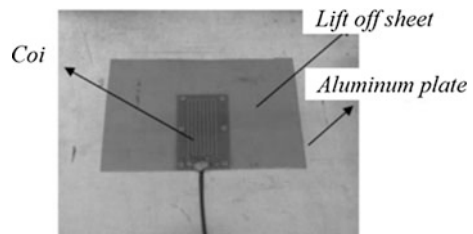
However, it is hard to obtain the expressions of magnetic flux density and eddy current in the time domain by calculating the IFT of (2.141) to (2.143) directly.

2.5.4 Example and Comparison of Results

In order to verify the effectiveness of the analytical expression and calculation, a complete EMAT model, comprising a square permanent magnet with a perpendicular magnetic field, was set up. The two-layer structure coil, with each layer having eight meander belts, is taken as an example to perform the calculation. The coil is placed above the specimen and the liftoff distance between the coil and specimen is achieved using the non-magnetic and non-conductive thin liftoff sheet. The value of the liftoff can be adjusted, as shown in Fig. 2.34.

In Fig. 2.34, the coil's dimension and material's parameters are shown in Tables 2.1 and 2.2. In the experiment, a radio frequency (RF) power amplifier (AG1024), which can provide a continuous sine signal and tone-burst signal, is supplied to the meander coil. This radio frequency power amplifier can not only generate a continuous sinusoidal signal, the frequency and amplitude of which is continuous and adjustable, but can also generate the tone-burst signal, whose frequency, amplitude, and cycle number are adjustable. In the experiment, the oscilloscope records the wave data used to measure the voltages of the coil and the $1\ \Omega$ sample resistance, which is connected in series with the coil. Thus, the current of the coil can be obtained according to the voltage of the sample resistance. The resistance and inductance of the coil can be calculated in terms of the measured continuous sine voltage and current signal.

Fig. 2.34 The setup of the experiment



In the calculation of the coil’s pulsed magnetic field, the pulsed excitation should be applied on the coil. The tone-burst voltage and current signals used for generating the acoustic waves can also be measured. When the liftoff value of the coil is 1 mm, a tone-burst signal with 500 kHz frequency is applied. The cycle number is 4. The voltage signal in the sample resistance (i.e., the coil’s current signal) is shown in Fig. 2.35.

In order to compare with the numerical computation methods, the TSFEM method is used for the calculation of the above model. Since the calculation of the 3D model is too complex, the influence of the coil’s end is neglected and it is assumed that the length of the coil and conductor are infinite in their length direction. The 2D model of the coil is calculated in this way. In the 2D model, the calculation can only obtain the y component of the eddy current, not the x component or z component of the magnetic flux density. The calculation is done using the finite element analysis software *Comsol Multiphysics*.

The current signal shown in Fig. 2.35 is used as the excitation in the simulation. Since the frequency of the excitation signal is very high, the skin depth is very small. Meanwhile, the dimensions of the coil conductor are also very small. In order to guarantee the accuracy of the results, it is necessary to draw a dense grid within the conductor’s skin depth and the coil conductors. The total number of elements in the TSFEM calculation model is 15,348, as shown in Fig. 2.36.

Fig. 2.35 Measured pulsed voltage and current signals

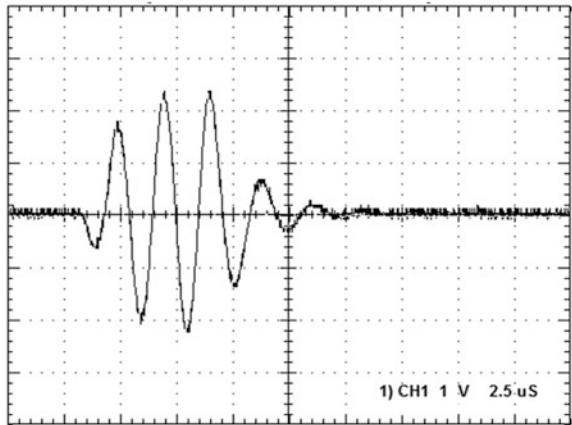
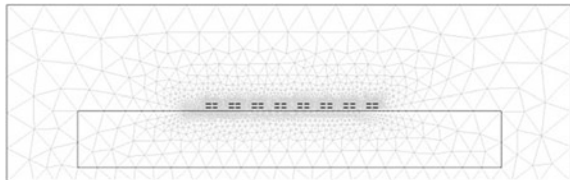


Fig. 2.36 The simulation model of TSFEM



Firstly, the coil's impedance under different liftoff values was calculated. According to (2.141), (2.142), and (2.143), a high-accuracy adaptive recursive *Simpson* method is used to calculate the numerical integration. Since the expression only contains the trigonometric function, but the *Bessel function* is included in the spiral coil's expression, the expression has a very good convergence, so the calculation is much simpler.

The FFT-IFFT method was used to calculate the coil's pulsed magnetic field and the inductive coil in the specimen. For the current signal in Fig. 2.36, 1024 points were selected to make the FFT process, substituting the amplitude corresponding to each frequency into (2.130), (2.131), and (2.132), and calculating the eddy current and magnetic induction intensity corresponding to each frequency using the recursive adaptive method. Finally, we obtain the time-domain signal of the eddy current and magnetic induction intensity by IFFT.

The analytical model's calculated value of the y component of eddy current density and the x and z components of magnetic induction intensity at the coordinates (1.1725 mm, 11.665 mm, -0.1 mm) is shown in Figs. 2.37, 2.38, and 2.39, respectively, as well as the calculated values by the TSFEM method. Figures 2.40 and 2.41 show the calculated values of the x and z components of the magnetic

Fig. 2.37 The y component of the eddy current density at the coordinates (1.1725 mm, 11.665 mm, -0.1 mm)

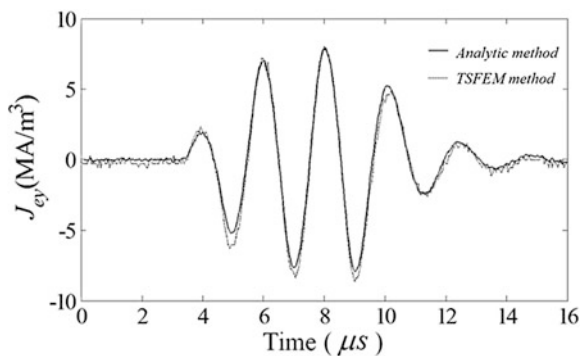


Fig. 2.38 The x component of the magnetic induction intensity at the coordinates (1.1725 mm, 11.665 mm, -0.1 mm)

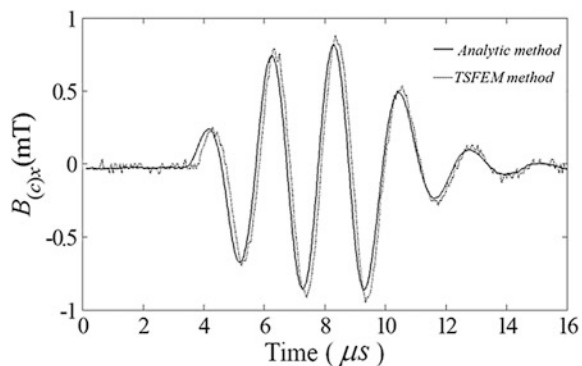


Fig. 2.39 The z component of the magnetic induction intensity at the coordinates (1.1725 mm, 11.665 mm, -0.1 mm)

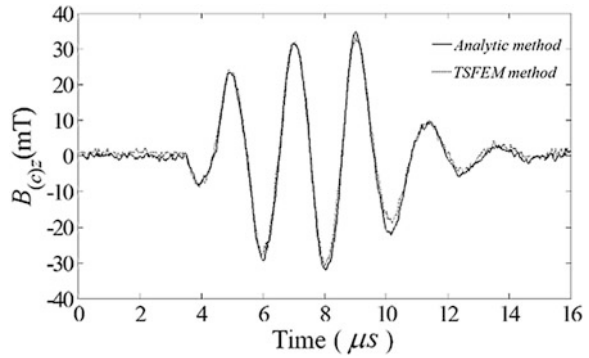


Fig. 2.40 The x component of the magnetic induction intensity at the coordinates (1.1725 mm, 11.665 mm, -0.1 mm)

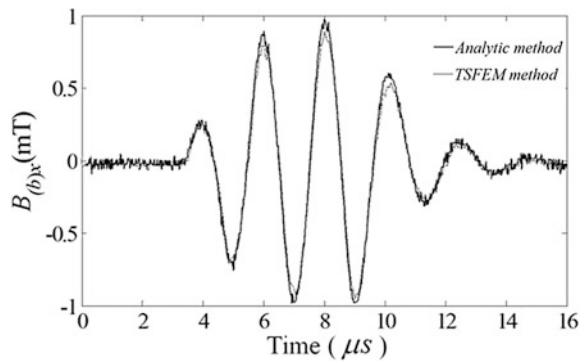
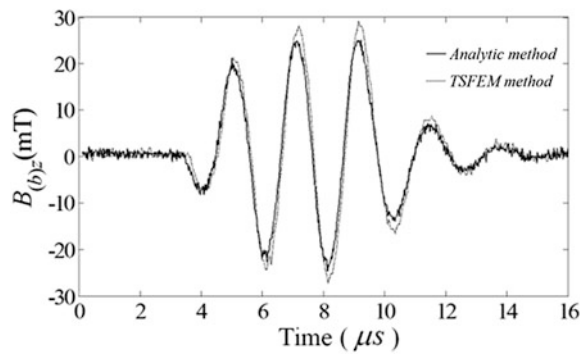


Fig. 2.41 The z component of the magnetic induction intensity at the coordinates (1.1725 mm, 11.665 mm, -0.1 mm)



induction intensity at the coordinates (1.1725 mm, 11.665 mm, -0.1 mm) by the analytical model and the TSFEM method. The horizontal axis in Figs. 2.37 and 2.39 represents the time. It can be seen from these pictures that there is basic agreement of time and amplitude of the calculated values between the analytical model and the TSFEM method, even if a certain error does exist.

Because the coil's skin effect and proximity effect are neglected in the derivation process of the analytical equation, inaccurate simulation results will definitely result between the analytical equation and the actual physical model with the assumption of equality of the current density in the conductor. Since it is difficult to evaluate the skin effect and proximity effect in the coil's analytical model, the neglecting of their effect is a general practice for the derivation of the coil's analytical model. The calculated error caused by this issue is, in general, acceptable in practical engineering applications. In addition, the concept of taking the meander coil equivalent to the superposition of the single fold closing coil itself can also bring about some calculation errors.

Compared with the numerical calculation, the advantages of the analytical calculation are the clarity of the analytic equation's physical meaning and the rapid calculation process.

2.6 The Analytical Method of EMAT Under Impulse Voltage Excitation [5]

In practical applications, most of the excitation power supply of EMAT is a voltage source or a power source. If the *Lorentz force* in EMAT can be calculated when the excitation of the pulsed voltage or power is given, it will be beneficial to the analysis and design of EMAT. Based on the analytic calculation of the EMAT coil impedance, the EMAT's analytical analysis method under voltage excitation can be obtained.

The EMAT analytic method of several coil structure's EMAT can be achieved when the pulsed current is given in advance. Actually, if the coil's terminal voltage or input power is already known, the pulsed voltage or power signal can be transformed into a pulsed current signal through the coil's impedance. Meanwhile, it can enable the analysis of EMAT by using the aforementioned method. Thus, the analytical problem of EMAT under the pulsed voltage can be transformed into the current excitation problem if the EMAT coil's voltage is given.

2.6.1 Calculating the Pulsed Current Using the Analytical Equation

In the sinusoidal steady state, if the excited voltage of the coil is given, the excited current of the coil can be expressed by (2.144).

$$I(\omega) = \frac{U(\omega)}{Z(\omega)} \quad (2.144)$$

For the pulse voltage excitation, the excitation of pulsed current can be calculated using the method of FFT-IFFT, specifically. Firstly, the pulsed voltage signal is transformed into frequency domain using FFT, according to (2.144), and the value of the current's frequency domain under a specific frequency is calculated. Then, IFFT is used to obtain the pulsed current of the time domain.

2.6.2 Calculating the Pulsed Current Using the Field-Circuit Coupling Finite Element Method

Using the field-circuit coupling method, the pulsed current is calculated. No matter what kind of voltage excitation is applied on the coil, narrow pulses, general tone-burst signals, or windowed tone-burst signals, the excitation signal can be expressed as the superposition of a series trigonometric function, as shown in (2.145).

$$u(t) = \sum_{k=1}^N U_k \cos(\omega_k t + \varphi_k) \quad 0 \leq t \leq T \quad (2.145)$$

In the above equation, $k = 1, 2, \dots, N$; U_k is the amplitude of the harmonic component of order k , ω_k is the angular frequency of the k th-order component; φ_k is the initial phase angle of the k th-order component, and T represents the duration of the excitation signal.

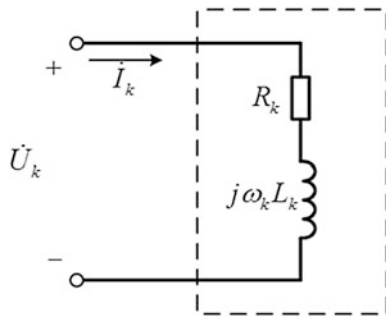
In (2.145), U_k , ω_k , and φ_k can be obtained using the FFT process. If the equivalent circuit parameters of the coil and specimen system can be calculated according to *Ohm's law*, the current excitation signal can be obtained through the IFFT process.

Since the frequency of the excitation signal is very high, the eddy current, skin, and proximity effects should be considered. Therefore, the alternating current (AC) resistance and inductance of the coil will change with the excitation frequency, the geometric configuration, and the electrical characteristics of the coils and the specimen.

For a specific frequency, the resistance and inductance of the coil can be calculated through sinusoidal steady-state analysis of the circuit-field coupling. For the system of the coil and specimen, the capacitance value is very small and can be neglected. Then, the system of the coil and specimen can be viewed as a two-port network, as in Fig. 2.42. The excitation voltage of EMATs is the port voltage, and the excitation current is the port current. Thus, the complex power can be expressed by (2.146).

$$\tilde{S}_k = \dot{\mathbf{U}}_k \dot{\mathbf{I}}_k^* = (R_k + j\omega_k L_k) \dot{\mathbf{I}}_k \dot{\mathbf{I}}_k^* = R_k I_k^2 + j\omega_k L_k I_k^2 \quad (2.146)$$

Fig. 2.42 Equivalent two-port network of coil



In the above equation, \tilde{S}_k represents the complex power, \dot{U}_k represents the port voltage, \dot{I}_k is the port current, \dot{I}_k^* is the conjugate of \dot{I}_k , and I_k is the effective value of \dot{I}_k . R_k and L_k are the equivalent resistance and inductance of the two-port network—the AC resistance and inductance of the coil.

Neglecting the displacement current in the coil and specimen field, we obtain the phasor notation of *Poynting theorem*, as shown in (2.147).

$$-\iint_S (\dot{E}_k \times \dot{H}_k^*) \cdot d\mathbf{s} = \iiint_V \frac{1}{\sigma} J_k^2 dV + j \iiint_V \omega \mu H_k^2 dV \quad (2.147)$$

In the above equation, \dot{E}_k is the electrical field strength phasor quantity, \dot{H}_k^* is the conjugate of the magnetic field intensity phasor quantity \dot{H}_k , J_k is the current density, and H_k is the magnetic field intensity. In (2.147), the left part of the equation represents the electromagnetic complex power flowing into the field close to the coil and specimen, the first term of the right part represents the dissipative active power and the second term of the right part represents dissipative reactive power.

Comparing (2.146) with (2.147), we obtain (2.148) and (2.149).

$$R_k = \frac{1}{I_k^2} \iiint_V \frac{1}{\sigma} J_k^2 dV \quad (2.148)$$

$$L_k = \frac{1}{I_k^2} \iiint_V \mu H_k^2 dV \quad (2.149)$$

In the above equations, ω is the angular frequency.

Therefore, when we calculate the impedance of the coil, we shall use the time-harmonic field equation, considering the eddy current effect, skin effect, and the proximity effect. By replacing the partial differential operator $\partial/\partial t$ with $j\omega$, the expression of the time-harmonic field equation can be converted into (2.150) and (2.151).

$$j\omega\sigma A - \frac{1}{\mu}\nabla^2 A = J_s \quad (2.150)$$

$$I = \iint_{\Omega_r} (J_s + J_e) ds \quad (2.151)$$

Correspondingly, we get (2.152), (2.153), and (2.154).

$$J_e = -j\omega\sigma A \quad (2.152)$$

$$J = J_s + J_e \quad (2.153)$$

$$H = \frac{1}{\mu} \nabla \times A \quad (2.154)$$

When J and H are determined, the resistance R_k and inductance L_k of the coil can be calculated according to (2.148) and (2.149).

When the pulsed excitation of the coil is calculated using the FFT-IFFT method, the characteristics of EMAT can be analyzed using the pulsed current, which was given in the preceding part of the text.

Using the circuit-field coupling FEM method, the simulation methods and calculated steps of the EMAT under the impulse voltage excitation are shown in Fig. 2.43.

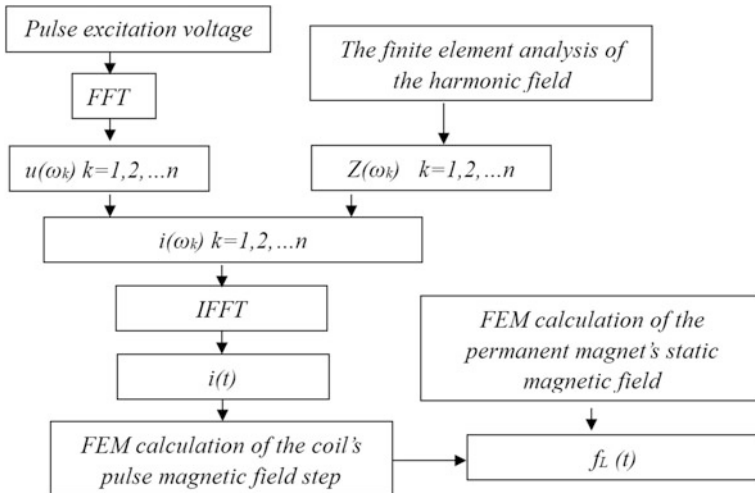


Fig. 2.43 The analytical procedure of EMAT under the pulsed voltage excitation

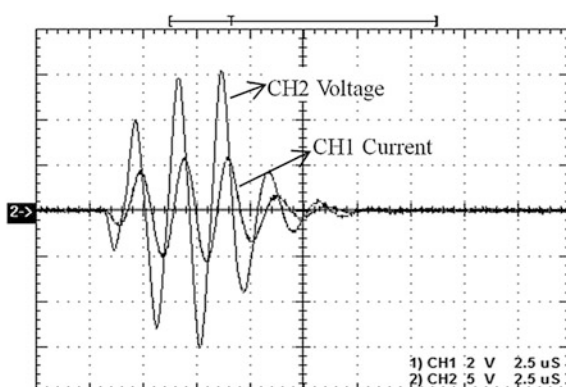
The given theoretical analysis method under the pulsed voltage of Lorentz force-based EMAT is also suited to the analysis of the EMAT based on the magnetostrictive mechanism

2.6.3 The Coil's Current Calculation Examples Realized Using the Circuit-Field Coupled Finite Element Method

Following the setup shown in Fig. 2.34, calculations and experimental work are performed. The parameters of the coil and the specimen are shown in Tables 2.1 and 2.2. In this work, the liftoff value between coil and specimen is 1 mm. In the experiments, the tone-burst signal was provided by RF power amplifier. An oscilloscope, which can record the wave data, was used to measure the voltages of the coil and 1 Ω sampling resistance, which was connected in series with the coil. The tone-burst signals with 500 kHz frequencies and 3 period number were supplied to the meander coil. The voltage and current signals used for generating the acoustic waves can also be measured, as shown in Fig. 2.44.

In the calculation process, the measured voltage signal in Fig. 2.44 was used as the pulsed voltage excitation. The signal was transformed into the frequency domain by FFT. After that, the coil inductance and resistance of each point can be calculated by the field-circuit coupled method. Then, the amplitude and phase position of the electric current of each frequency point were calculated. Finally, the time-domain waveform of the pulsed current was obtained by IFFT. The time-domain pulsed current can be taken as the excitation source of the simulated analysis for EMAT.

Fig. 2.44 The measured pulsed voltage and current signals of the coil



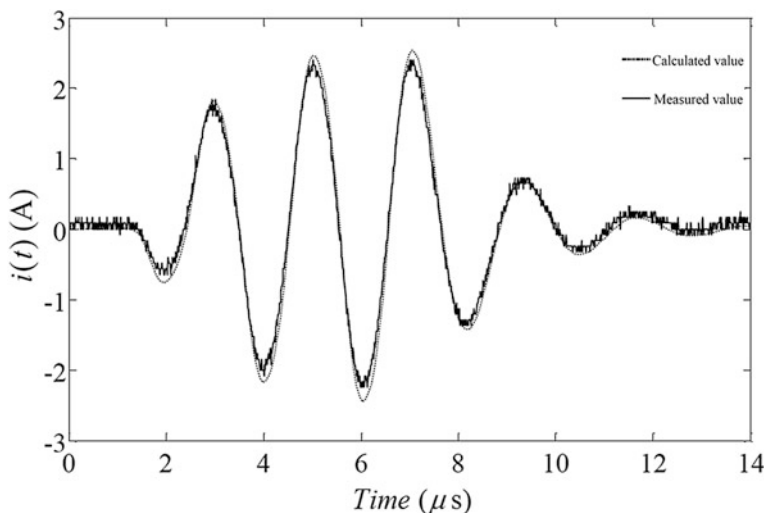


Fig. 2.45 The calculated and measured current signals

The calculated and experimental measured current signals at the liftoff distance of 1 mm are shown in Fig. 2.45. Comparing these two waveforms, we find that both the amplitudes and phase positions are in agreement, which verifies the validity of the proposed field-circuit coupled and FFT-IFFT method, and impedance calculation equations.

References

1. Hao, K., Huang, S., Zhao, W., et al.: Analytical calculation and analysis for meander-coil electromagnetic acoustic transducers. In: 2011 IEEE International Instrumentation and Measurement Technology Conference, I2MTC 2011—Proceedings, pp. 231–234
2. Hao, K., Huang, S., Zhao, W., et al.: Modeling and finite element analysis of transduction process of electromagnetic acoustic transducers for nonferromagnetic material testing. *J. Cent. S. Univ. Technol.* **18**(3), 749–754 (2011)
3. Hao, K., Huang, S., Zhao, W., et al.: Analytical modeling and calculation of pulsed magnetic field and input impedance for EMATs with planar spiral coils. *NDT & E Int.* **44**(3), 274–280 (2011)
4. Hao, K., Huang, S., Zhao, W., et al.: Analytical modelling and calculation of impedance and pulsed magnetic field for rectangular meander coil based on second order potential. *Acta Phys. Sin.* **60**(7), 078103 (2011) (in Chinese)
5. Hao, K., Huang, S., Zhao, W., et al.: Circuit-field coupled finite element analysis method for an electromagnetic acoustic transducer under pulsed voltage excitation. *Chin. Phys. B* **20**(6), 791–800 (2011)

Electromagnetic Ultrasonic Guided Waves

Huang, S.; Wang, S.; Li, W.; Wang, Q.

2016, XII, 301 p. 292 illus., Hardcover

ISBN: 978-981-10-0562-6